Redox-dependent hydrogen bond network rearrangement of Ferredoxin-$NADP^+$ reductase revealed by high-resolution X-ray and neutron crystallography

A Doctoral Thesis

By

Midori Uenaka

Submitted to
The Graduate School of Science, Osaka University

January, 2025

ACKNOWLEDGMENTS

This study was conducted under the supervision of Professor Genji Kurisu at the Institute for Protein Research, Osaka University. I would like to express my deepest gratitude to him for his invaluable support, constructive guidance, and insightful comments, which were instrumental throughout the course of my study.

I am also sincerely grateful to Associate Professor Hideaki Tanaka, formerly of the Institute for Protein Research, Osaka University (currently affiliated with TechnoPro, Inc., TechnoPro R&D Company), for his significant contributions and valuable advice during my research.

I extend my heartfelt appreciation to the staff of the Ibaraki Prefectural Local Government Beam Line (iBIX) at J-PARC MLF, Tokai, Ibaraki, Japan, as well as to Prof. Katsuhiro Kusaka and Dr. Naomine Yano, for their kind assistance during the data collection, which was conducted under the proposal numbers 2020PX2010, 2021PX2013, 2021PX2002, 2022PX2002, and 2022B0042.

I am equally grateful to the staff of BL26B2, BL41XU, and BL44XU at SPring-8, Hyogo, Japan, for their invaluable support during the data collection conducted under the proposal numbers 2022B2557, 2022A6500, 2022B6500, 2023A6500, 2023B6500, and 2024A6500.

I would like to express my sincere gratitude to Professor Atsushi Nakagawa and Associate Professor Eiki Yamashita of the Institute for Protein Research, Osaka University, for their meticulous review of my dissertation and their constructive feedback.

My deepest thanks also go to Dr. Takeshi Murakawa (Faculty of medicine, Osaka Medical and Pharmaceutical University) for his invaluable support in crystallization for neutron crystallography. I am equally grateful to Dr. Taro Tamada and Dr. Yu Hirano (Institute for Quantum Life Science, National

Institutes for Quantum Science and Technology) for their kind guidance and invaluable advice on the processing and refinement of neutron diffraction data.

I would like to express my deep gratitude to the anonymous reviewers of my submitted papers and Professor Nakagawa, the editor. Without their support, I would not have been able to even prepare for my doctoral defense.

This work was supported by JST SPRING, Grant Number JPMJSP2138, for which I am profoundly grateful.

I would also like to express my heartfelt gratitude to my friends who shared the journey through our doctoral programs with me. Their unwavering moral support and warm encouragement have been an indispensable source of strength.

Finally, I would like to thank all members of the Kurisu Lab for their helpful support and camaraderie throughout my doctoral studies.

January 2025

Midori Uenaka

Protein Crystallography Laboratory

Department of Biological Sciences

Graduate School of Science

Osaka University

Contents

I. INTRODUCTION

Photosynthesis is a collective term for metabolic reactions driven primarily by light energy. Essential elements that constitute life, such as carbon, nitrogen, and sulfur, predominantly exist in oxidized forms on Earth. Therefore, organisms must reduce and assimilate inorganic oxides to utilize organic compounds such as sugars and amino acids. In oxygenic photosynthesis, performed by higher plants, algae and cyanobacteria, light energy harvested during photosynthesis is used to synthesize organic compounds from inorganic oxides. Consequently, the existence of reductive assimilation enzymes driven by photosynthetic energy is indispensable. In higher plants, the conversion of light energy into chemical energy occurs in the thylakoid membrane through two membrane protein complexes: Photosystem II (PSII) and Photosystem I (PSI). Within these photosystems, charge separation reactions are initiated by light excitation. These two photosystems are connected in series via several electron transfer proteins and are sequentially excited by light, enabling the acquisition of exceptionally high reducing power. In PSII, electrons obtained from oxidization of the water are utilized to reduce plastoquinone (PQ). Reduced PQ then transfers electrons and protons to the cytochrome b_6f complex, creating a proton gradient across the thylakoid membrane. This gradient drives ATP synthesis through ATP synthase. The electrons in the thylakoid membrane are further transferred from the cytochrome b_6f complex to PSI via plastocyanin (PC). After being re-excited by light in PSI, the electrons are ultimately transferred to ferredoxin (Fd), a small iron-sulfur protein that acts as an electron carrier. This sequential process of charge transfer is known as the photosynthetic electron transport chain.

The reducing power transferred to Fd is distributed among multiple Fd-dependent enzymes, which drive the reductive assimilation reactions

essential for synthesizing organic molecules. Electron transfer reactions, in addition to their role in photosynthesis, are critical to other fundamental metabolic pathways such as respiration and drug metabolism. These reactions involve a series of oxidation-reduction processes mediated by electron carriers, which are predominantly proteins containing cofactors or prosthetic groups. In electron transfer reactions, high efficiency and specificity are required to rapidly transfer electrons between the redox centers of different proteins. Factors such as redox potential, protein-protein interactions, and the distance of electron transfer are considered critical determinants. However, controlling the flow of electrons within and between molecules remains a significant challenge even in modern science and technology. Understanding how proteins achieve these chemical reactions efficiently within living organisms is crucial for advancing scientific and technological fields.

In the photosynthetic electron transport chain, as described earlier, the reducing power generated from light energy is ultimately transferred to Fd, which then distributes it among various Fd-dependent enzymes. Plant-type Fd, found widely in photosynthetic organisms including higher plants and cyanobacteria, contains a [2Fe-2S] cluster as its redox center. Fd functions as a single-electron carrier, receiving a electron from PSI and transferring it to Fd-dependent enzymes. Known Fd-dependent enzymes include ferredoxin-$NADP^+$ reductase (FNR, involved in carbon assimilation), sulfite reductase (SiR, involved in sulfur assimilation), nitrite reductase (NiR, involved in nitrogen assimilation), glutamate synthase (GOGAT, involved in nitrogen), and ferredoxin-thioredoxin reductase (FTR, involved in regulation of Calvin-Benson-Bassham cycle or ATP synthase) (1-3). In addition to these enzymes involved in inorganic assimilation, recent studies have identified Fd-dependent enzymes involved in various metabolic processes. These include desaturases responsible for fatty acid desaturation (4), choline

monooxygenase for betaine synthesis (5), and heme oxygenase for phytochrome synthesis (6), indicating that Fd plays a role in a diverse array of metabolic reactions.

Among these enzymes, ferredoxin-$NADP^+$ reductase (FNR) is the primary consumer of reducing power derived from Fd in chloroplasts and cyanobacteria. FNR is a flavoenzyme that contains a non-covalently bound flavin adenine dinucleotide (FAD) as its prosthetic group. It catalyzes the redox reaction between Fd and NADP(H) in plastids. The redox-active component of FNR is the isoalloxazine ring of FAD, which functions as a two-electron donor/acceptor, cycling through three states: fully oxidized (quinone state), semiquinone, and fully reduced state (hydroquinone state) (**Figure 1**). In higher plants, tissue-specific isoforms of FNR are distributed across various organs. Leaf-type FNR (L-FNR) is found in photosynthetic tissues such as leaves, while root-type FNR (R-FNR) is distributed in non-photosynthetic tissues such as roots and fruits (7,8). L-FNR participates in the photosynthetic electron transfer, where it receives electrons from PSI via Fd and reduces $NADP^+$ to produce NADPH. The generated NADPH is utilized in the Calvin-Benson-Bassham (CBB) cycle for carbon fixation.

Other non-photosynthetic tissues like roots and fruits lack the ability to use light-derived reducing power. Instead, R-FNR in root plastids oxidizes NADPH, generated through the oxidative pentose phosphate pathway, to $NADP^+$, transferring the resulting electrons to Fd. These electrons are then supplied to Fd-dependent enzymes such as NiR and SiR, which are involved in nitrogen or sulfur assimilation (9-11). Previous studies have reported that the interaction affinity between maize R-FNR and its corresponding Fds differs significantly depending on the type of Fd. For instance, R-FNR binds to non-photosynthetic Fd (Fd-III) from root plastids with a binding constant approximately ten times higher than that for photosynthetic Fd (Fd-I) (7). This finding suggests that photosynthetic and non-photosynthetic Fd-FNR

pairs interact through distinct modes, reflecting possible tissue- or organ-specific adaptations in redox metabolism pathways.

Electron transfer between Fd and Fd-dependent enzymes has been extensively studied using biochemical and biophysical approaches. These studies reveal that no consensus sequence or motif specific to Fd-dependence exists. Instead, the amino acid residues on the surface of Fd critical for forming electron transfer complexes differ among partner enzymes (2,12-15). X-ray crystallography, NMR spectroscopy, and thermodynamic analyses of Fd and Fd-dependent proteins have shown that these proteins transiently form specific 1:1 complexes mediated primarily by electrostatic interactions under *in vitro* conditions (16-19).

For R-FNR, a structural study under non-physiological conditions reported the crystal structure of a complex between oxidized Fd and oxidized R-FNR at a resolution of 2.50 Å (PDB ID: 5H5J) (17). This study identified the amino acid residues involved in electrostatic interactions between Fd and R-FNR. However, while it is known that the complex dissociates rapidly after electron transfer, the mechanism by which transient complexes initiate dissociation remains unclear. In the case of photosynthetic Fd and FNR derived from *Equisetum arvense*, the *K*m value for the reaction between reduced Fd and oxidized FNR is 0.62 μM, while that between oxidized Fd and reduced FNR is 11.4 μM, indicating a marked change in affinity following electron transfer (20, 21). Nevertheless, earlier structural studies of Fd-FNR complexes could not elucidate the molecular basis for redox-dependent interaction changes.

High-resolution X-ray structures of L-FNR and R-FNR in complex with nicotinamide cofactors ($NADP^+$ or NADPH) have clarified the mechanism of hydride transfer between NAD(P)H and FAD (22, 23). However, due to the limitations of X-ray crystallography, the positions of hydrogen atoms could not be determined in these studies. Hydrogen atoms, with only one

electron, produce significantly weaker scattering signals compared to heavier atoms such as carbon, nitrogen, and oxygen. To visualize hydrogen atoms coupled with reduction of FAD, a resolution better than 1.2 Å is typically required. Achieving such high resolution often necessitates intense X-ray exposure, which can damage crystals or inadvertently reduce redox proteins during data collection (24, 25). As an alternative, neutron crystallography offers a powerful method for determining the positions of hydrogen (H) and deuterium (D) atoms in protein structures. Neutrons interact with atomic nuclei rather than electrons, allowing scattering signals from hydrogen and deuterium to be comparable to those of heavier atoms (26).

Although the reduction of FAD involves the addition of two hydrogen atoms to the isoalloxazine ring at N1 and N5, most studies on redox-dependent structural changes in FNR have focused on the carbon, nitrogen, and oxygen atoms of the isoalloxazine ring. Consequently, critical structural factors related to redox-dependent affinity changes between FNR and Fd remain poorly understood. In this study, to investigate the structural changes associated with the reduction of the FAD isoalloxazine ring in greater detail, we conducted X-ray crystallographic analysis of R-FNR from maize root under carefully controlled redox conditions. Using high-quality crystals, we experimentally confirmed how the structure of FNR changes with the redox state of FAD. Given that the two-electron reduction of FAD results in only minor chemical changes in the isoalloxazine ring, we also employed neutron crystallography to complement X-ray data and visualize proton positions, which are crucial for understanding the electron transfer mechanism.

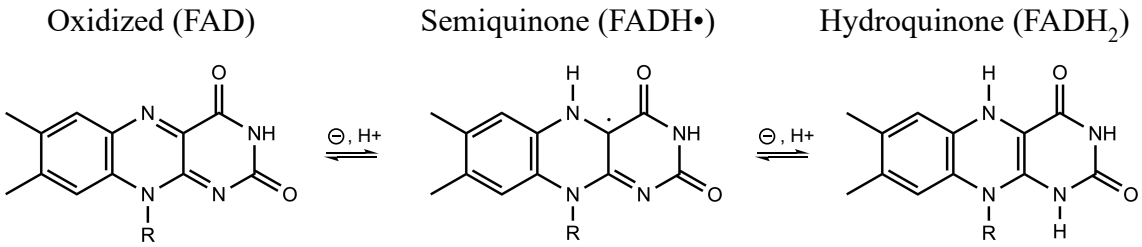

Figure 1. Redox States of Isoalloxazine ring in FAD

FAD (Flavin Adenine Dinucleotide) exists in three distinct redox states. The biochemical roles of FAD vary depending on these redox states.

II. X-RAY CRYSTALLOGRAPHY OF OXIDIZED AND REDUCED FNR CONSIDERING THE X-RAY IRRADIATION DEPENDENT REDUCTION

2-1 General outline

In general, high-resolution data acquisition in X-ray crystallography requires extensive X-ray irradiation to the crystal. However, it has been previously reported that X-ray irradiation induces the generation of hydrated electrons, which can reduce redox-active centers such as metal atoms in the active sites of proteins (24, 25). In the case of the redox enzyme such as ferredoxin-$NADP^+$ reductase (FNR), excessive X-ray irradiation to the oxidized crystals may also lead to partial reduction of redox centers. Despite this, none of the FNR X-ray structures reported in the Protein Data Bank (PDB) to date have accounted for the extent of X-ray exposure during data collection. To accurately understand the structural changes between the oxidized and reduced states, it is essential to conduct X-ray crystallographic analyses that mitigate radiation damage and reflect the true oxidized state.

In this study, to analyze the true oxidized structure, I determined the relationship between X-ray dose and the reduction rate of FAD. Diffraction data were collected using the minimum X-ray exposure required to limit the reduction rate to below 10%. As a result, the X-ray structure of oxidized FNR with FAD was determined at a resolution of 1.15 Å. Additionally, the structure of reduced FNR, confirmed to be in a fully oxidized hydroquinone state of FAD ($FADH_2$) using a microspectrophotometer, was determined at a resolution of 1.10 Å.

Comparison of the two structures revealed no significant changes in the main-chain structure. However, analysis of the F_o - F_o difference Fourier

maps calculated using structure factors from the oxidized and reduced states showed that structural changes existed and were concentrated around FAD, including its surrounding side chains and water molecules. Upon reduction of FAD to $FADH_2$, structural changes were observed in the side chains of Arg115 and Ser95, as well as in the C-terminal region of Tyr317. Changes in the number and arrangement of water molecules around these regions were also identified.

2-2 Material and methods

Culture of Root-FNR from *Maize* (R-FNR)

Recombinant Root-FNR (R-FNR) from maize was overexpressed in *Escherichia coli*. A freeze-stock of *E. coli* host BL21 (DE3) cells transformed with pQE-60, into which R-FNR had been cloned by a predecessor in our laboratory, was used for cultivation. All glassware and media were autoclaved at 121 °C for 20 minutes prior to use. LB medium was used for cultivation, and the typical culture volume was 8 liters. In a clean bench, a flame-sterilized inoculation loop was used to transfer a loopful of the freeze-stock into 100 mL of LB medium containing sodium ampicillin at a final concentration of 0.1 mg/mL. The culture was incubated at 37 °C and shaken at 180 rpm for 17 hours (pre-culture) using a Taitec BioShaker BR-23FP. A 300 mL Erlenmeyer flask was used as the cultivation vessel for this step. Next, 10 mL of the pre-culture was transferred into 1 L of LB medium containing sodium ampicillin at a final concentration of 0.1 mg/mL. Eight 3 L baffled flasks were prepared, each containing 1 L of medium. The cultures were incubated at 37 °C and shaken at 120 rpm for 2 hours and 30 minutes until the optical density at 600 nm (OD600) reached 0.5–0.6. At this point, 1 mL of 1 M IPTG was added to achieve a final concentration of 1 mM, and the cultures were incubated at 30 °C and shaken at 100 rpm for 20 hours using a Taitec BioShaker G・BR-200. The cultures were then transferred to 1 L centrifuge bottles and centrifuged at 4 °C and 8000 rpm for 10 minutes using a Beckman JLA-9.1000 rotor. The supernatant was discarded, and the cell pellets were resuspended in PBS (phosphate-buffered saline). The resuspended cells were transferred to multiple 50 mL centrifuge tubes (Sumilon Tube PP) and centrifuged again to collect the cell pellets, which were then frozen in liquid nitrogen and stored in a -80 °C freezer. Additionally, 0.5 mL of the pre-culture was mixed with 0.1 mL of sterile 80%

(v/v) glycerol, frozen in liquid nitrogen, and stored as a freeze-stock in a -80 °C freezer.

Purification of R-FNR

The following purification procedures were performed on cell pellets obtained from 4 L of culture. The frozen cell pellet was thawed under running water and resuspended in 200 mL of resuspension buffer in a 200 mL plastic beaker. To this, 1 mL of 100 mM PMSF solution (final concentration: 0.5 mM) and 200 μL of 2-mercaptoethanol (final concentration: 0.1% (v/v)) were added. Cell disruption was performed using a SONIFIER 450 ultrasonic homogenizer (BRANSON ULTRASONICS). The cells were sonicated for 3 minutes (output control: 5, duty cycle: 50%), followed by 2 minutes of cooling, then sonicated again for 2 minutes with another 2 minutes of cooling. This cycle was repeated twice, followed by an additional 2 minutes of sonication. To prevent overheating, all operations were performed in an ice bath with stirring. The lysate was ultracentrifuged at 4 °C and 40,000 rpm for 20 minutes (HITACHI himac CP80WX, P45AT rotor), and the supernatant was collected. To this supernatant, 20 mL of DEAE-cellulose resin (DE52), pre-equilibrated with resuspension buffer, was added and stirred at 4 °C for 5 minutes to adsorb impurities. The resin was packed into an open column, and the non-adsorbed fraction (flow-through) was collected. Ammonium sulfate was added to the flow-through to achieve 35% saturation, and the solution was stirred for 5 minutes, followed by centrifugation at 4 °C and 13,000 g for 20 minutes (TOMY, AR 500-04 rotor). The resulting pellet, which contained impurities other than R-FNR, was discarded, and the supernatant was collected. To remove suspended particles that could not be eliminated by centrifugation, the supernatant was filtered using a disk filter (HV Filter, unit 0.45 μm, PVDF membrane 33 mm, Millex). Ammonium sulfate was then added to the collected supernatant to achieve

70% saturation. After stirring for 5 minutes, the solution was centrifuged again at 4 °C and 13,000 g for 20 minutes. The resulting pellet was dissolved in 80 mL of resuspension buffer and placed into a dialysis membrane (SnakeSkin™ Thermo Fisher Scientific, molecular weight cutoff: 10 kDa). The sample was dialyzed against 5 L of dialysis buffer at 4 °C with gentle stirring overnight. The dialysis buffer was replaced with fresh buffer 4 hours after dialysis began. The dialyzed sample was centrifuged at 4 °C and 13,000 g for 20 minutes, and the supernatant was filtered through a disk filter (HV Filter, unit 0.22 μm, PVDF membrane 33 mm, Millex). The sample was then applied to a DEAE-Toyopearl anion exchange column (bed volume: 120 mL), pre-equilibrated with 2 CV of A buffer (50 mM Tris-HCl, pH 7.5). Non-adsorbed fractions (crude FNR fraction) were collected during column washing. The collected fraction was applied to a Blue Sepharose 6 Fast Flow anion exchange resin column (150 mL), pre-equilibrated with 2 CV of A buffer. The FNR was eluted with a gradient from A buffer to B buffer (50 mM Tris-HCl, pH 7.5, 1 M NaCl) at a flow rate of 7 mL/min. Eluted fractions containing FNR were identified by UV absorption at 280 nm and the characteristic yellow color of FNR, and these fractions were collected. SDS-PAGE was performed on each eluted fraction, and fractions showing bands near molecular weights of 32 kDa were collected. The collected fractions were concentrated to below 5 mL using an ultrafiltration membrane with a molecular weight cutoff of 30 kDa (Millipore, Amicon Ultra-15) and centrifugation at 4 °C and 4,000 rpm (Beckman Coulter, Allegra X-30R Centrifuge). The concentrated sample was applied to a Sephacryl S-100 gel filtration column (16/60), pre-equilibrated with 1.25 CV of gel filtration buffer (50 mM Tris-HCl, pH 7.5, 150 mM NaCl), and FNR was eluted with 1.5 CV of gel filtration buffer. The eluted fractions containing FNR were identified by UV absorption at 280 nm and the characteristic yellow color, and these fractions were collected. The collected fractions were further

concentrated to 60 mg/mL using an ultrafiltration membrane with a molecular weight cutoff of 30 kDa and centrifugation at 4 °C and 4,000 rpm. The resulting sample was designated as the final purified FNR standard.

Crystallization and Cryoprotection of $wtFNR_{oxi}$

The R-FNR crystal was initially obtained using the hanging drop vapor diffusion method. The protein stock solution was diluted to a concentration of 30 mg/mL in a buffer containing 50 mM Tris-HCl (pH 7.5) and 150 mM NaCl. It was then mixed with an equal volume of a precipitant solution (0.2 M 2-(N-morpholino) ethane sulfonic acid (MES), pH 6.0, and 24.6% PEG 2000) and equilibrated against the precipitant solution at 20 ºC. All crystals used for X-ray diffraction experiments were prepared using the batch method with micro-seeds. The micro-seed solution was prepared by breaking a macro-scale R-FNR crystal (~300 μm) in a stabilization buffer (0.24 M MES, pH 6.4, and 29.5% PEG 2000) using a Seed Beads™ Kit (Hampton Research). The crystallization drops for the batch method with micro-seeds were prepared by mixing 1 μL of R-FNR solution (30 mg/mL in 50 mM Tris-HCl, pH 7.5, and 150 mM NaCl buffer), 0.8 μL of precipitant solution (0.195 M MES, pH 6.0, and 23.985% PEG 2000), and 0.2 μL of the micro-seed solution diluted in stabilization buffer. The drop was then completely covered with paraffin oil and incubated at 20 ºC. After 2–3 days, crystals of approximately 300 × 300 × 100 μm^3 were obtained. The crystals were soaked in a cryoprotectant containing 0.24 M MES, pH 6.4, 15% PEG 2000, and glycerol. The glycerol concentration was initially 1% and was increased by 1% every 5 minutes until reaching 20%. The crystals were then mounted using a CryoLoops™ (Hampton Research) and cryocooled in liquid nitrogen.

Preparing Reduced R-FNR Crystals ($wtFNR_{red}$) via Dithionite soaking

All steps described in this section were performed in an anaerobic chamber. All liquids and crystallization drop containing R-FNR crystals were stored under anaerobic conditions for one day prior to starting the experiment. An oxidized R-FNR crystal (~300 × 300 × 100 μm³) was soaked in 50 μL of a dithionite-containing buffer (5 mM sodium dithionite, 0.2 M MES, pH 6.0, and 15% glycerol) for 5.5-6 hours. The reduced crystal was then mounted using a CryoLoops™ (Hampton Research) and cryocooled in liquid nitrogen. The absorption spectrum of the reduced R-FNR crystal mounted on the cryo-loop was measured using an offline micro-spectrophotometer of BL26B2 at SPring-8/RIKEN, equipped with a DT-Mini and SD2000 (Ocean Optics Inc.) (27, 28).

X-ray Diffraction experiment and analysis

X-ray diffraction experiments were conducted at BL44XU of SPring-8 using an EIGER X 16M detector to detect diffraction spots. A focused X-ray beam (λ=0.9000 Å) was used for these diffraction experiments. The beam size was adjusted using a 50 μm pinhole, and the beam flux was attenuated with a 1.6 mm aluminum foil. According to the master thesis submitted to Graduate School of Science, Osaka University, in 2019 by Ms. Akane Ise from my laboratory, it was necessary to reduce the X-ray dose to less than 0.11 MGy in order to reduce the reduction rate to less than 10%. Therefore, multiple X-ray irradiation points were set within a single crystal, and diffraction intensity data were collected so that the reduction rate at each irradiation point was less than 10%. The absorbed dose was calculated using RAD-DOSE 3D (29). This allowed diffraction intensity data to be collected with a maximum dose of 0.097 MGy. To prevent X-ray radiation damage, data were collected from six non-overlapping points of a single crystal. X-ray data collection started from one end of the crystal. A total of 200 images covering 20° of rotation were collected from a single assigned point. The

measurement point was then moved 60 µm towards the opposite end, and another 20 images were collected from a fresh part of the crystal as shown in **Figure 2**. This process of crystal movement and data collection was repeated until the entire angular range was covered using six assigned exposure points. All images were processed with XDS (30), and the six datasets were scaled and merged using XSCALE. Data collection statistics were calculated with AIMLESS (35). Initial phase information was obtained using molecular replacement in PHASER (31), with the crystal structure of R-FNR (PDB ID: 5h59) used as the search model. Iterative refinement of XYZ coordinates, real-space refinement, isotropic B-factor refinement, TLS refinement, and manual model correction was performed starting from the initial model using phenix.refine (32, 33) and COOT (34). The F_o(wtFNR$_{oxi}$)−F_o(wtFNR$_{red}$) difference maps were generated with FFT in the CCP4 program suite (35) using phase angles calculated from the final refined structure against the oxidized dataset to confirm structural differences between the two datasets.

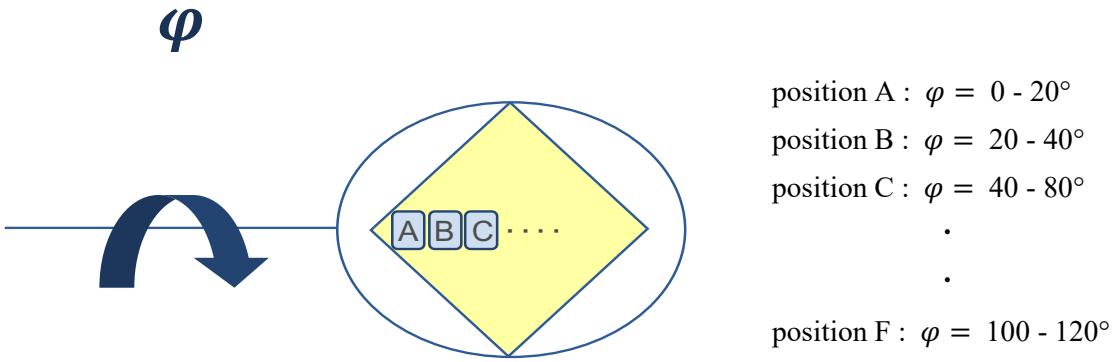

Figure 2. X-ray data collection strategy for low dose data sets.

Six data collection points separated enough were assigned. One set was collected starting from different angles of 0, 20, 40, 60, 80 and 100 degrees each.

2-3 Results

Preparation of recombinant R-FNR protein in two redox states

Recombinant wild-type R-FNR protein (wtFNR) were successfully produced using a synthetic gene with altered codon usages optimized for expression in *E. coli*. In the final purification step of gel filtration, R-FNR eluted as a single peak (Figure 3). The purified R-FNR protein showed typical spectra of FAD and migrated in SDS–PAGE as homogeneous bands, which means that the obtained R-FNR samples were highly pure oxidized FNR, $wtFNR_{oxi}$ (Figure 4).

The absorption spectrum of chemically reduced R-FNR exhibits a characteristic peak at approximately 420 nm, which means FAD was fully reduced to be $FADH_2$. Spectroscopic measurements using a micro-spectrophotometer revealed a single peak around 420 nm in these crystals, confirming that the wtFNR was fully reduced to the two-electron reduced state, $wtFNR_{red}$ (Figure 5).

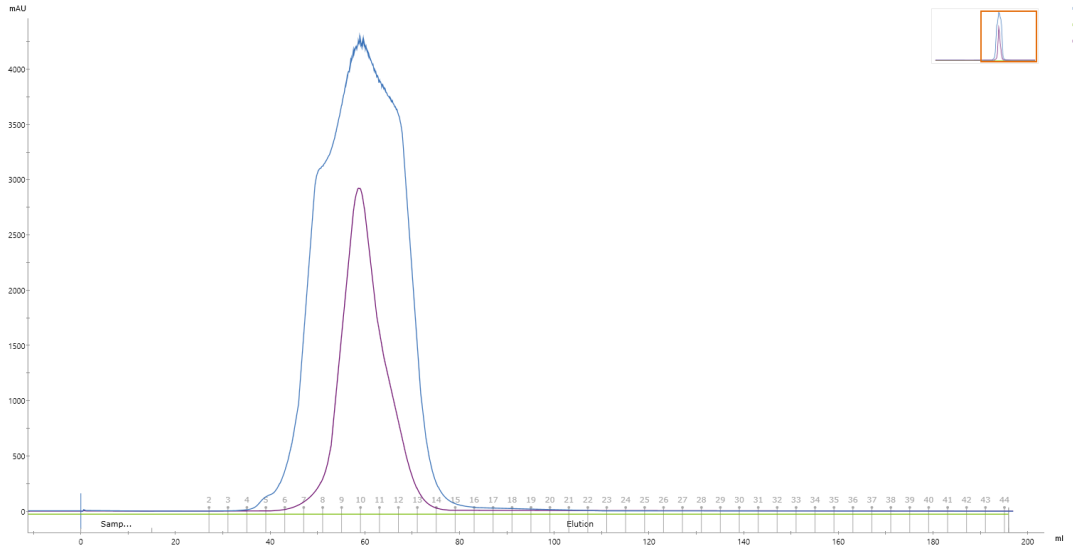

Figure 3. The elution profile from gel filtration column of $wtR\text{-}FNR_{oxi}$ at 280 (blue) and 460 (purple) nm.

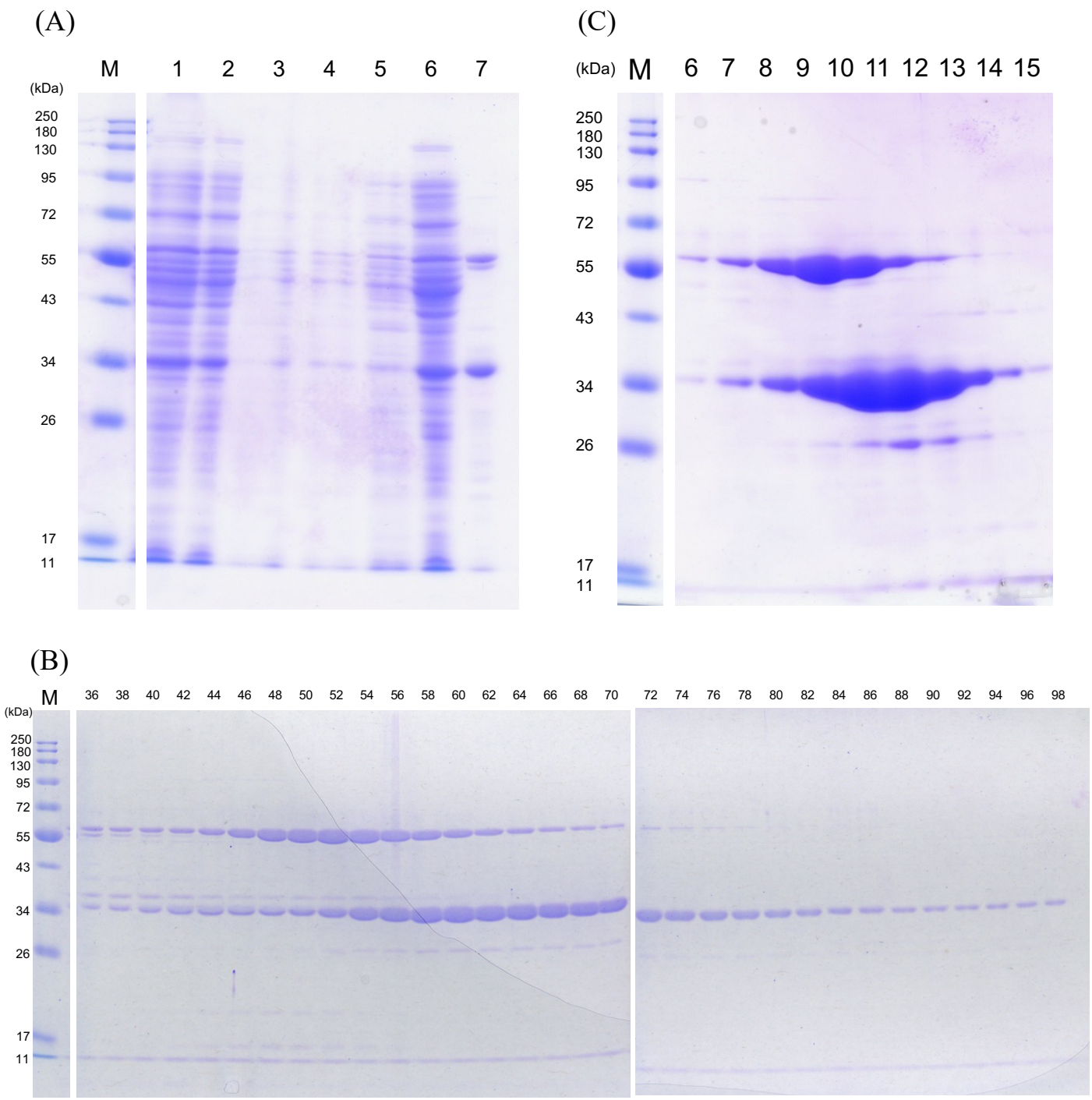

Figure 4. The results of SDS PAGE. M : Blue Prestained Protein Standard, Broad Range (BioLads), (A) 1: the supernatant after ultra-centrifuge **2**: DE52 flow through, 3: Ammonia sulfate suspension buffer, **4**: Ammonia sulfate precipitation, **5**: After dialysis buffer, 6: DEAE elution, **7**: DEAE flow through. (B) Elution of Blue Sepharose 6 Fast Flow. (C) Elution of Sephacryl Sepharose S-100 16/60.

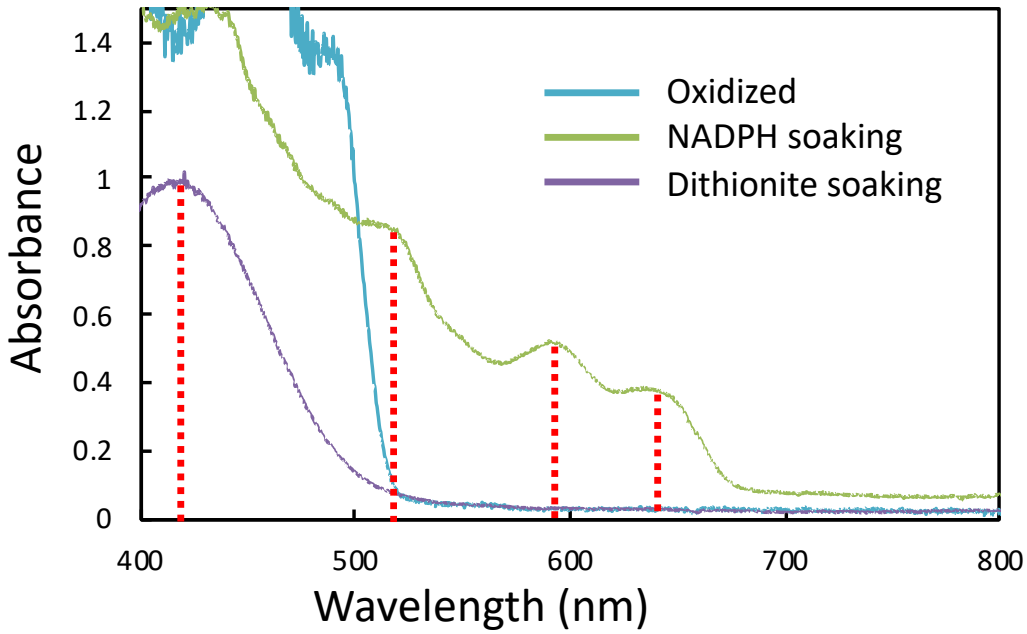

Figure 5. Absorption spectra of the R-FNR crystals by micro-spectrophotometry.
Absorption spectra of the R-FNR crystals with/without 5 mM dithionite and 20 mM NADPH. Ultraviolet region (<400 nm) was not shown due to the high absorbance from added dithionite. The red dashed lines indicate the characteristic peak positions in the spectra corresponding to each state.

Overall difference between oxidized and reduced R-FNR structure

Crystal structures of R-FNR oxidized and fully reduced form were successfully determined with the molecular replacement method using the 1.65 Å resolution structure of R-FNR (PDB:ID 5h59) previously registered in the PDB as a search model. Statistics of data collection, structure determination and crystallographic refinement for oxidized and reduced R-FNR are shown in Table 1. For each data set, one molecule was contained in the crystallographic asymmetric unit. Crystals of both oxidized wild-type FNR ($wtFNR_{oxi}$) and reduced wild-type FNR ($wtFNR_{red}$) were determined to

have the same space group, $P3_221$, with no significant differences in their unit cell parameters. The X-ray structures of $wtFNR_{oxi}$ and $wtFNR_{red}$ were refined to resolutions of 1.15 Å and 1.10 Å, respectively. The structures were refined until the crystallographic R-factors converged. The resolution achieved for the $wtFNR_{oxi}$ structure in this study (1.15 Å) is higher than that of previously reported oxidized FNR structures available in the Protein Data Bank (PDB), which range from 1.351 Å to 1.953 Å (e.g., PDB IDs 5h59, 5vw3, 5vw4, 5vw5, 5vw6, 5vw8, 5vw9, 5vwa, 5vwb). A comparison of the overall structures of $wtFNR_{oxi}$ and $wtFNR_{red}$ is shown in **Figure 6**. The root-mean-square deviation (r.m.s.d) of Cα atoms (residues 9–317) between $wtFNR_{oxi}$ and $wtFNR_{red}$ was 0.121 Å, indicating minimal structural differences at the backbone level (calculated with Lsqkab in CCP4). At the backbone level, the structures of the oxidized and reduced states were nearly identical, leading to the conclusion that reduction had minimal impact to the main chain structures.

Multi-conformation of Reduced $FADH_2$

The electron density map of $wtFNR_{red}$ indicated that $FADH_2$ was disordered. Even after the anisotropic temperature factors were introduced into FAD and refined, a difference map was still observed, so it was judged to be a dual conformer (**Figure 7**). Then, the $FADH_2$ was modeled as dual conformers, conformer A and B. The occupancy of conformer A, the major conformer of $FADH_2$, was refined to 60% occupancy. The isoalloxazine ring of conformer B, the minor conformer of $FADH_2$, was displaced by 0.6 Å apart relative to that of conformer A. When compared to $wtFNR_{oxi}$ that had only one conformer of FAD, the FAD conformation in $wtFNR_{oxi}$ closely resembles that of conformer A in $wtFNR_{red}$. The structural model of $wtFNR_{red}$ with dual conformers is shown in **Figure 8**.

Table 1. Crystallographic data and refinement statistic for X-ray structures

	X-ray Oxidized form	X-ray Reduced form
Data-collection statistics		
Beamline	SPring-8 BL44XU	SPring-8 BL44XU
Wavelength (Å)	0.90000	0.90000
Space group	$P3_221$	$P3_221$
Unit cell *a, b, c* (Å) α, β, γ (°)	59.29, 59.29, 187.22, 90, 90, 120	59.08, 59.08, 186.90, 90, 90, 120
Temperature (K)	100	100
Resolution (Å)	45.02-1.15 (1.17-1.15)[1]	44.879-1.10 (1.12-1.10)[1]
Total reflections	849232 (27008)[1]	1003869 (48755)[1]
Unique reflections	136343 (6686)[1]	154288 (7518)[1]
R_{merge}	0.101 (0.351)[1]	0.119 (0.441)[1]
R_{meas}	0.109 (0.404)[1]	0.129 (0.480)[1]
R_{pim}	0.042 (0.195)[1]	0.049 (0.186)[1]
$CC_{1/2}$	0.995 (0.895)[1]	0.992 (0.901)[1]
Mean $I/\sigma(I)$	10.1 (3.1)[1]	9.1 (3.6)[1]
Completeness (%)	99.9 (99.8)[1]	100.0 (100.0)[1]
Multiplicity	6.2 (4.0)[1]	6.5 (6.5)[1]
Wilson *B*-factor (Å^2)	9.2	9.7
Refinement		
Resolution (Å)	45.02-1.15 (1.17-1.15)[1]	44.879-1.10 (1.12-1.10)[1]
No. of reflections	136335	154328
R_{work}	0.1409	0.1425
R_{free}	0.1572	0.1552
R.m.s.d. from ideal geometry		
Bond lengths (Å)	0.007	0.0054
Bond angles (°)	0.940	0.975
Ramachandran plot		
Most favored (%)	98.00	100.00
Allowed (%)	2.00	0.00
Outliers (%)	0.00	0.00
PDB code	9KKG	9KKH

[1] Statistics in parentheses represent values calculated from the highest resolution shell.

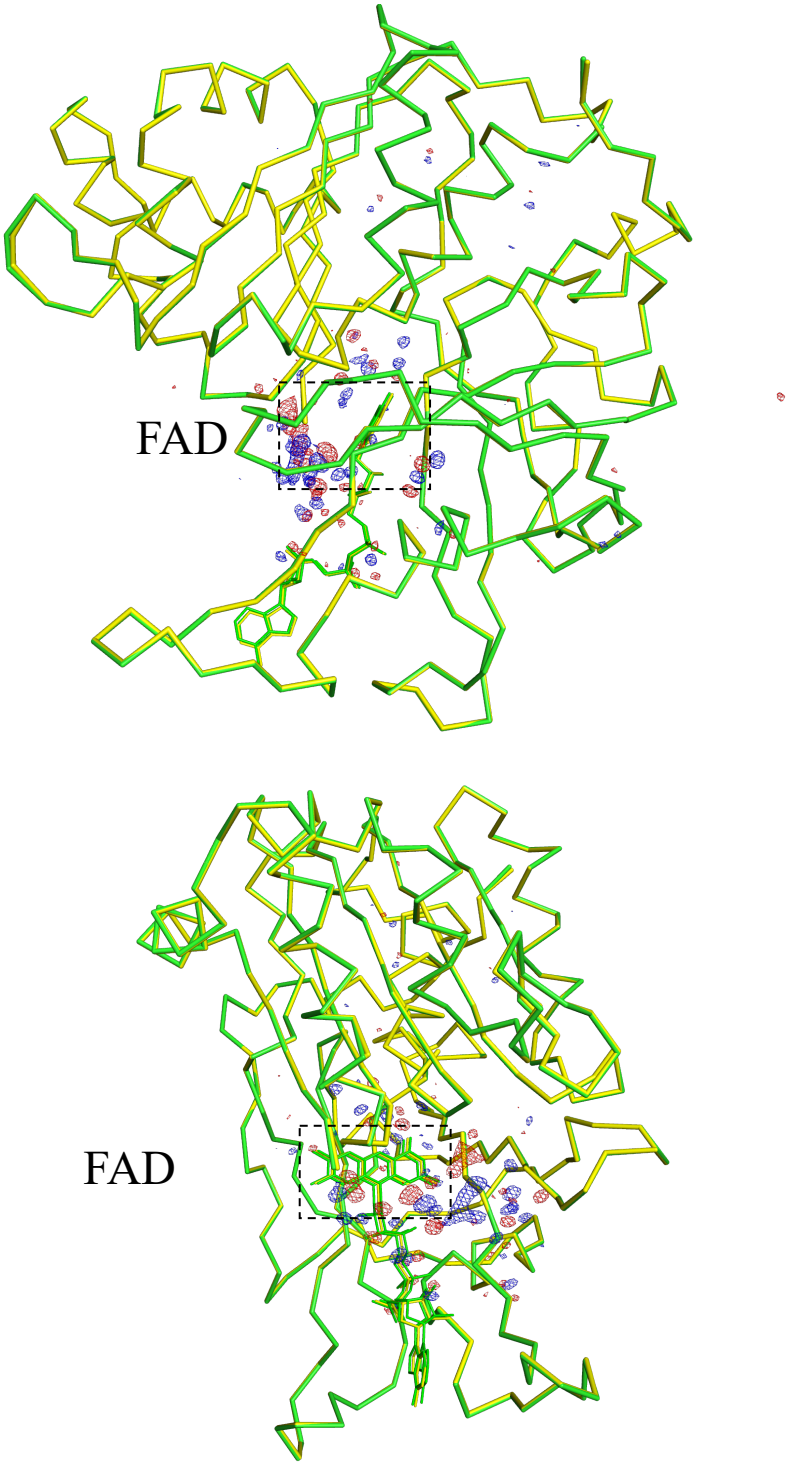

Figure 6. Comparison of the overall structures of oxidized (green) and reduced (yellow) R-FNR. Each model was aligned based on the positions of all Cα atoms (backbone r.m.s.d. = 0.121 Å). The green and red meshes represent the F_o(wtFNR$_{oxi}$)−F_o(wtFNR$_{red}$) difference map contoured at +4.0σ and -4.0σ, respectively. The figure in the lower part is the upper figure rotated 90 degrees in the X-axis direction.

(A)

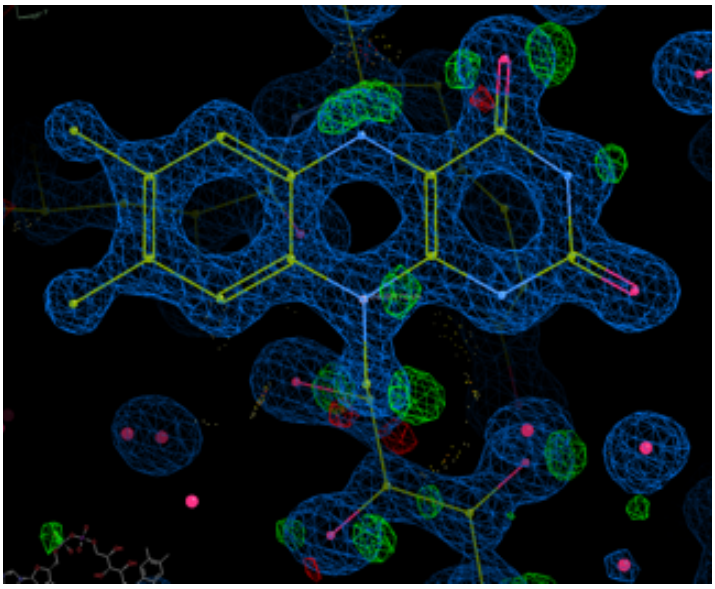

(B)

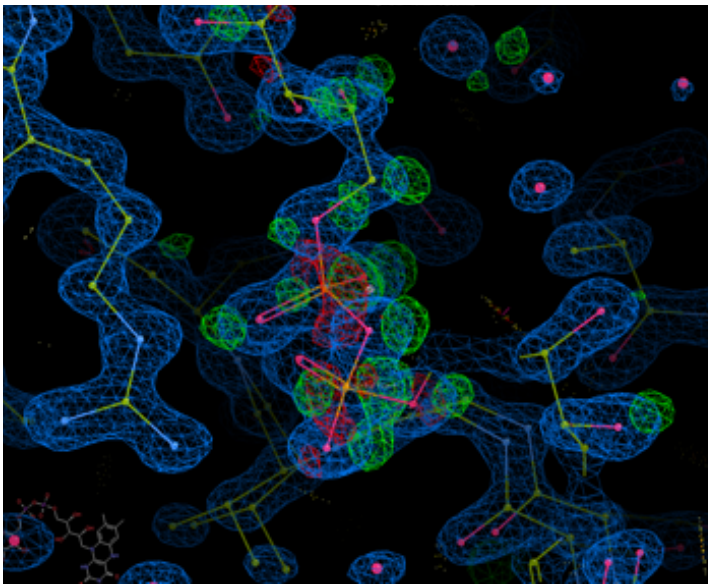

Figure 7. X-ray electron density map after refinement using anisotropic B-factors. Refined with Phenix. Only FAD was selected as Anisotropic atoms in individual ADP tab. 2mFo-DFc X-ray electron density map 2.5 sigma, blue mesh. Fo-Fc omit maps of positive (green) and negative (red) peaks at counter levels of 3.52 sigma value were illustrated using Coot. (A) Around the isoalloxazine ring of FAD (B) Around the phosphoric acid of FAD.

2-4 Discussion

Comparing the structures of the oxidized and reduced forms, the root-mean-square deviation (r.m.s.d) of the Cα atoms (residues 9–317) between them was 0.121 Å, indicating that the backbone structures of the two forms were nearly identical and that reduction had minimal effects at the main chain level.

The oxidized and reduced form crystal exhibited minimal changes in space group and unit cell parameters, indicating that the crystals were isomorphous. Thus, the difference Fourier method was applied to compare the subtle structural changes between them. For the F_o(wtFNR$_{oxi}$)−F_o(wtFNR$_{red}$) difference Fourier phase calculation, the oxidized structure with a lower R-factor was used. A comparison of the oxidized and reduced X-ray structures of FNR is shown in Figure 6. The mesh density represents the F_o-F_o difference Fourier map, where blue mesh indicates electron density lost upon reduction, and red mesh represents electron density gained upon reduction. Since minimal changes were observed in the backbone structure, the difference map showed the structural changes of side chain or water molecule that were concentrated around the FAD molecule. This indicates that the minimal structural changes in the backbone suggest FNR maintains a stable overall structure while regulating redox reactions through a flexible local environment.

Analysis of the F_o(wtFNR$_{oxi}$)−F_o(wtFNR$_{red}$) difference Fourier map revealed that structural changes caused by side chains and water molecules were concentrated around FAD. Due to the prominence of these changes, an enlarged view of the isoalloxazine ring region of FAD is shown in Figure 8. The difference map highlights structural changes around the C-terminal tyrosine residue (Tyr317), the arginine residue (Arg115), and nearby water molecule which are shown in Figure 8. Upon reduction, the side chain of

Arg115 reoriented, moving away from FAD. This reorientation was accompanied by increased flexibility, resulting in the disappearance of electron density for most of the side chain, except for the Cβ and Cγ atoms (Figure 9). Furthermore, this change in the orientation of the Arg115 side chain led to the appearance of two new water molecules, HOH616 and HOH618. The carboxyl group of Tyr317 at the C-terminus shifted inward upon reduction, with the OXT atom moving by 0.84 Å. The OXT atom formed a hydrogen bond with HOH281 as a donor. Interestingly, HOH281 moved inward by 1.78 Å upon reduction, and this inward shift of HOH281 caused HOH169 to be displaced outward by 2.03 Å (Figure 8). These shifts are likely due to the reduction of FAD to $FADH_2$, as HOH78 moved 1.18 Å closer to the N1 nitrogen atom of FAD and formed a new hydrogen bond with it. This new interaction likely disrupted the hydrogen bond network involving HOH169, forcing it to move outward. The analysis of water molecule behavior around FAD revealed that not all water molecules moved during the redox transition. Notably, no significant movement was observed in HOH27, HOH60, and HOH20.

These findings suggest that the reduction of FAD induces complexed changes in the hydrogen-bond network of surrounding water molecules, which in turn influence nearby amino acid residues. However, the exact mechanism linking these changes to the reduction of FAD to $FADH_2$ remains unclear, and it can only be speculated that these changes result from alterations in the hydrogen bonding between water molecules and $FADH_2$. Since the positions of hydrogen atoms cannot be determined solely from X-ray crystallographic data, further discussion on the detailed hydrogen-bonding interactions is not possible within this chapter.

Oxidized FAD

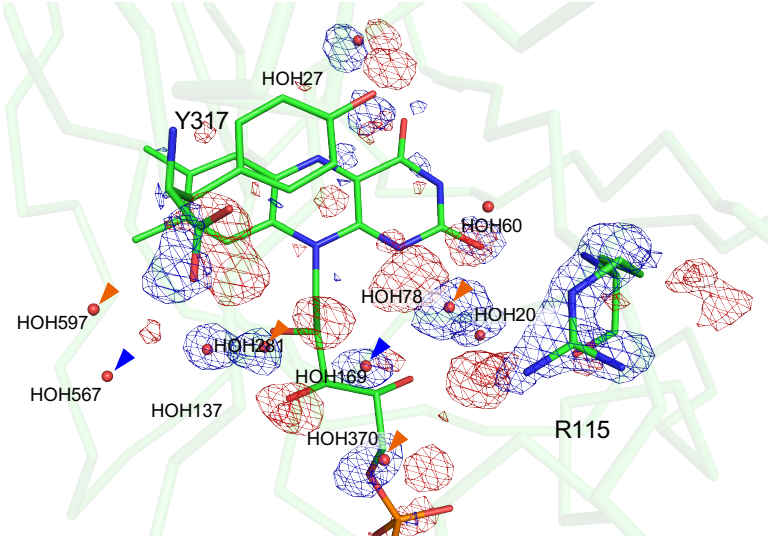

Reduced $FADH_2$

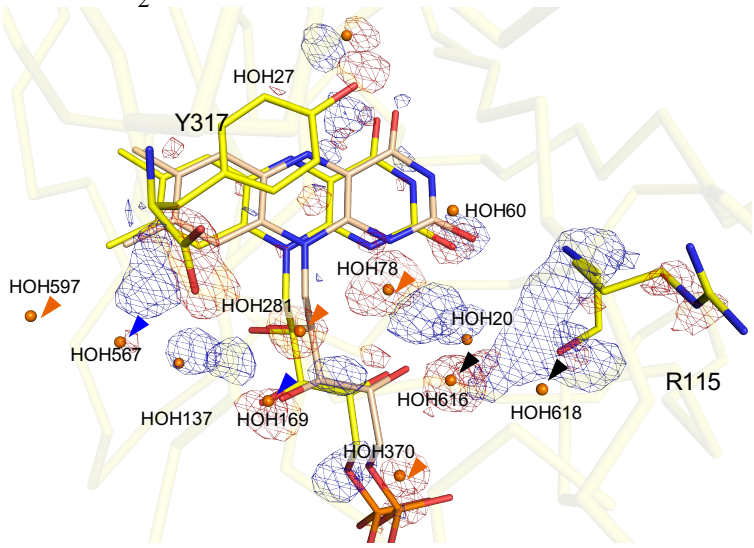

Figure 8. Enlarged views around FAD/$FADH_2$. The upper panel shows the oxidized model with the difference map, while the right panel displays the reduced model with the same difference map. In the lower panel, Conformer A of $FADH_2$ is shown in yellow, and Conformer B in pale orange. Orange arrows indicate moving water molecules. Among these, blue arrows highlight water molecules that shifted by more than 2 Å, and black arrows represent newly appearing water molecules.

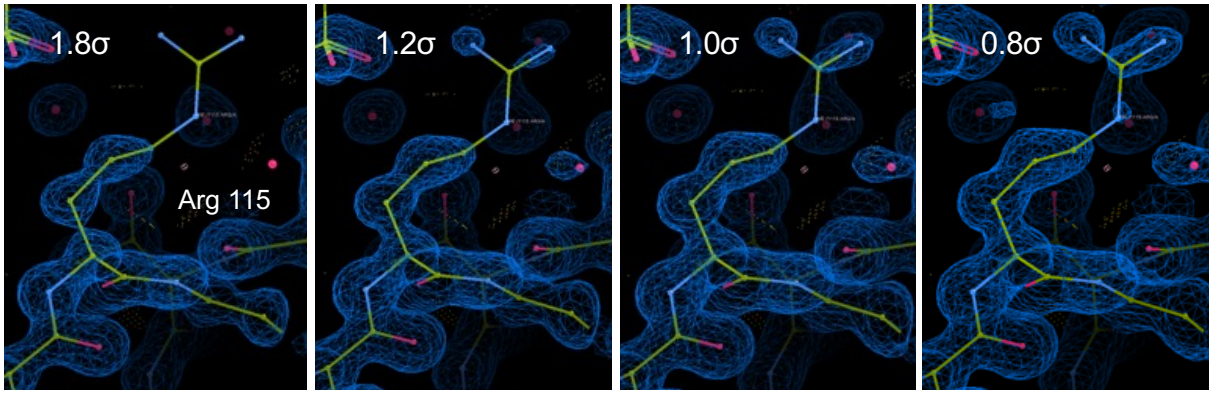

Figure 9. Electron density of R115 in the reduced X-ray structure. X-ray electron density map (blue mesh) at counter levels of indicated sigma value were illustrated using Coot.

III. NEUTRON CRYSTALLOGRAPHY OF OXIDIZED AND REDUCED FNR

3-1 General outline

In Chapter 2, high-resolution X-ray crystallographic analyses of oxidized and reduced FNR structures faced a limitation to precisely identify the positions of hydrogen atoms. Consequently, subtle structural changes, including hydrogen bonding networks dependent on the redox state of FNR, could not be elucidated. Determining all atomic coordinates, including hydrogen atoms, is therefore essential for accurately understanding the redox reactions of FNR. To address this limitation, I aimed to employ neutron crystallography—a powerful method for visualizing hydrogen atoms—to determine precise all atomic coordinates for oxidized and reduced FNR and compare their structures. This approach sought to reveal the structural changes associated with FNR redox states and to elucidate the mechanisms underlying efficient electron transfer.

Hydrogen atoms are critical for numerous protein reactions, interactions, and functional mechanisms. Determining the positions of hydrogen atoms and protons within proteins is crucial for accurately understanding protein properties and enzymatic reactions. However, as hydrogen atoms are light elements with only one electron, their electron density is difficult to observe using conventional X-ray crystallography, making precise position determination challenging. In contrast, neutron crystallography uses neutrons, which interact with atomic nuclei rather than electrons. This enables the direct observation of atomic nuclei, allowing hydrogen atoms and their isotope, deuterium, to be observed as readily as heavier atoms such

as carbon, nitrogen or oxygen. As a result, neutron crystallography provides a powerful means of accurately determining the positions of hydrogen atoms.

Despite its significant advantage in determining hydrogen atom positions, neutron crystallography remains underutilized. As of January 2025, only 232 protein structures out of approximately 229,000 deposited in the Protein Data Bank (PDB) have been determined using neutron crystallography. This limited application is primarily due to the technical challenges associated with the method.

One of the major challenges is the requirement for large crystals. The flux of neutron beams is relatively low, resulting in much weaker diffraction intensities compared to X-rays. This necessitates the use of protein crystals with a minimum volume of 1 mm^3 for neutron crystallographic analysis. However, producing protein crystals of this size using standard techniques is both difficult and time-consuming. Even if large crystals are successfully obtained, their size makes them more prone to damage during manipulations such as soaking or freezing, which further increases the complexity of experimental procedures. Additionally, data collection in neutron diffraction experiments requires significantly more time due to the weak diffraction intensities. While synchrotron-based X-ray diffraction experiments can collect a full dataset within approximately three minutes, neutron diffraction experiments typically require around 10 days.

Another key challenge is the necessity of sample deuteration in neutron crystallography. Neutrons exhibit strong incoherent scattering when interacting with hydrogen atoms, which increases background noise during diffraction measurements. To improve the quality of neutron diffraction data, it is essential to replace hydrogen atoms in the sample with deuterium, which has much lower incoherent scattering. However, fully deuterating a protein sample is associated with significant costs, further complicating the process.

Given these challenges, this study focused on optimizing conditions to reproducibly obtain large protein crystals and conducted neutron diffraction experiments using deuterium-substituted samples. These efforts aimed to overcome the inherent difficulties of neutron crystallography and to provide precise structural insights into the redox-dependent conformational changes in FNR.

3-2 Material and methods

Deuterium Exchange of R-FNR

After gel filtration, the final purified sample was concentrated to 0.5 mL using an ultrafiltration membrane. To this sample, 5 mL of deuterium gel filtration buffer (50 mM Tris-HCl, pH 7.5, 150 mM NaCl in D_2O) was added, and the sample was centrifuged (4 °C, 4000 rpm) until the volume was reduced to 0.5 mL (Beckman Coulter, Allegra X-30R Centrifuge). This process was repeated three times to achieve deuterium exchange of the FNR sample. The protein concentration of the obtained sample was determined by measuring absorbance at 460 nm, using a molar extinction coefficient of ε_{460}nm = 10 $mM^{-1}cm^{-1}$. The sample was rapidly frozen in liquid nitrogen and stored at -80 °C.

Crystallization to obtain large crystals of R-FNR

For neutron crystallographic analysis, protein crystals with a volume of at least 1 mm^3 are required. However, obtaining crystals of this size using standard methods is highly challenging. Through extensive optimization, a reproducible method for growing large crystals was established by combining micro-seeding and batch crystallization techniques. Additionally, since neutrons undergo strong incoherent scattering by hydrogen atoms, resulting in significant background noise during diffraction measurements, it was necessary to replace hydrogen atoms in the sample with deuterium. From this point onward, all crystallization reagents, including cryoprotectants, were deuterated to ensure successful neutron diffraction experiments.

Preparation of Seed Crystal Solution

A few single crystals (approximately 0.2 × 0.2 × 0.2 mm^3) obtained via conventional vapor diffusion method were transferred into 10 µL of stabilization buffer A in a hollow glass container and finely crushed using a needle. The entire suspension was transferred to a Seed Bead tube (HAMPTON RESEARCH), vortexed for 30 seconds, and cooled on ice for 30 seconds. This cycle was repeated six times. The resulting microcrystal suspension (hereafter referred to as the seed solution) was diluted using stabilization buffer A to prepare seed solutions with dilution factors of 10, 10^2, 10^3, 10^4, 10^5, and 10^6 (Figure 10). For crystallization, 1 µL of 30 mg/mL R-FNR, 0.8 µL of reservoir solution B, and 0.2 µL of the seed solution were mixed on a well of an MRC Under Oil Crystallization Plate (HAMPTON RESEARCH). The mixture was overlaid with 35 µL of paraffin oil and incubated statically at 20 °C overnight.

Table 2. Buffer composition used for crystallization.

Stabilization buffer A	0.24M MES (pD 6.81) PEG 2000 29.5% (w/v)
Reservoir solution B	0.195M MES (pD 6.41) PEG 2000 24.0% (w/v)

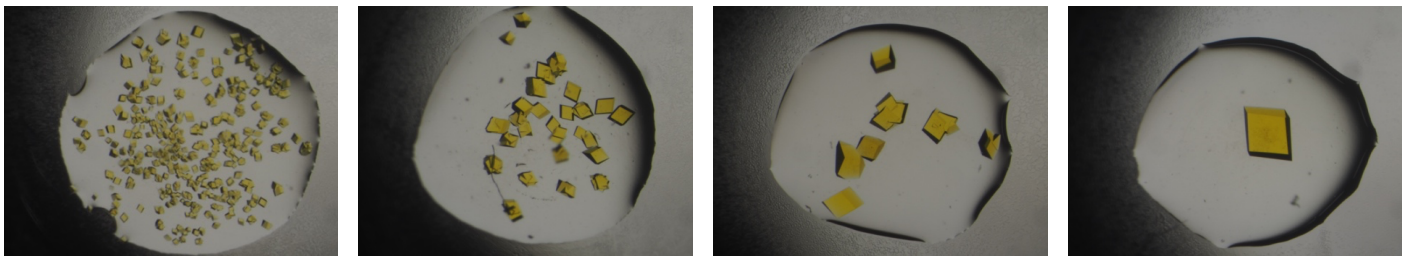

Figure 10. Estimation of the number of seed crystals in the seed solution. From left to right: 10^3 seed solution, 10^4 seed solution, 10^5 seed solution, 10^6 seed solution.

Preparation of a Large Crystal of wtFNR$_{oxi}$ for Neutron Crystallography

A large crystal of wtFNR for neutron crystallography was prepared using the batch method with micro-seeds. For neutron diffraction experiments, scale-up crystallization of R-FNR was performed using the batch method. A silicone-treated 6 mm × 30 mm Durham tube (Maruemu) was prepared, into which 300 µL of Fluorinert was added. Fluorinert, an inert solvent with a specific gravity of 1.7, is denser than the crystallization solution and does not mix with it. This layer of Fluorinert prevents crystals from adhering to the Durham tube and promotes free growth. The crystallization solution was gently layered on top of the Fluorinert. The purified protein solution was exchanged into a buffer containing 50 mM Tris-HCl (pD 7.91) and 150 mM NaCl in D_2O and diluted to 30 mg/mL. The crystallization solution for the batch method with micro-seeds was prepared by mixing 100 µL of R-FNR solution (30 mg/mL in 50 mM Tris-HCl, pD 7.91, and 150 mM NaCl buffer in D_2O), 80 µL of precipitant solution (0.195 M MES, pD 6.41, and 23.985% PEG 2000 in D_2O), 18.8 µL of stabilization buffer, and 0.2 µL of microseed solution diluted in stabilization buffer. To prevent evaporation of the crystallization solution, 200 µL of paraffin oil was layered on top (**Figure 11A, B: Left**). To flatten the crystallization interface and ensure proper crystal growth, 100 µL of Fluorinert was carefully removed from the bottom layer using a pipette tip inserted into the Fluorinert layer. The setup was then incubated at 20 °C for 2–3 weeks to allow crystal growth. Single crystals with sizes ranging from approximately 2 to 5 mm³ were obtained (**Figure 12**).

For further scaling up and producing even larger crystals, crystallization was conducted in 11 mm × 60 mm ultracentrifuge tubes (Ultra-Clear Centrifuge Tubes, BECKMAN COULTER). Prior to use, the tubes were cut to approximately 50 mm in height. Into the ultracentrifuge tube, 1.5 mL of

Fluorinert was added. The crystallization solution was prepared by mixing 240 µL of R-FNR solution (30 mg/mL in 50 mM Tris-HCl, pD 7.91, and 150 mM NaCl buffer in D_2O), 192 µL of precipitant solution (0.195 M MES, pH 6.0, and 23.985% PEG 2000 in D_2O), 47.8 µL of stabilization buffer, and 0.2 µL of microseed solution diluted in stabilization buffer. To prevent evaporation of the crystallization solution, 200 µL of paraffin oil was layered on top (**Figure 11B, right**). Similar to the Durham tube setup, 0.5 mL of Fluorinert was carefully removed using a pipette tip to flatten the crystallization interface. The tube was incubated at 20 °C for 2–3 weeks, during which crystals formed. If the incubation period exceeded three weeks, the crystals began to develop cracks. Therefore, crystals needed to be frozen within three weeks. On average, crystals with sizes of 4–5 mm^3 were obtained when the incubation period was set to three weeks.

To obtain smaller crystals of 1–2 mm^3, the incubation period could be shortened to 1–2 weeks, or the number of nuclei could be adjusted by varying the dilution ratio of the seed solution added to the Durham tube to achieve 3–4 nuclei. This approach allowed the production of crystals of the desired size.

(A)

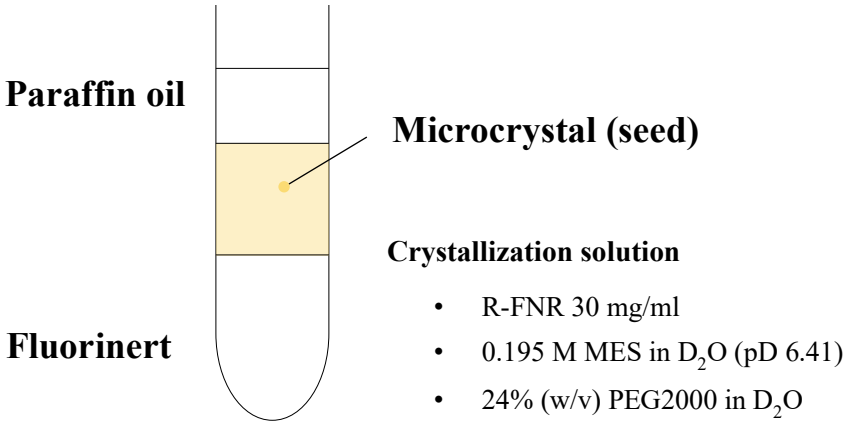

(B)

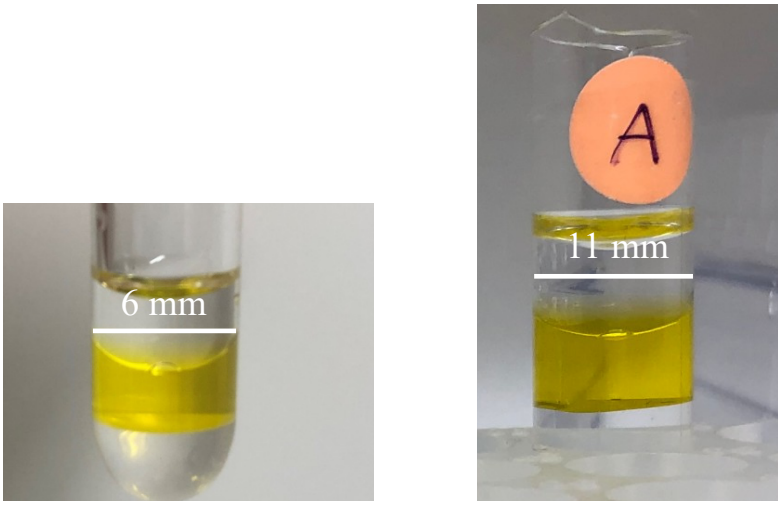

Figure 11. Crystallization by batch method with seed crystals to obtain large crystals.

(A) Diagram of crystallization and crystallization conditions. (B) Left: Crystallization using a Durham tube Right: Crystallization in ultracentrifuge tubes.

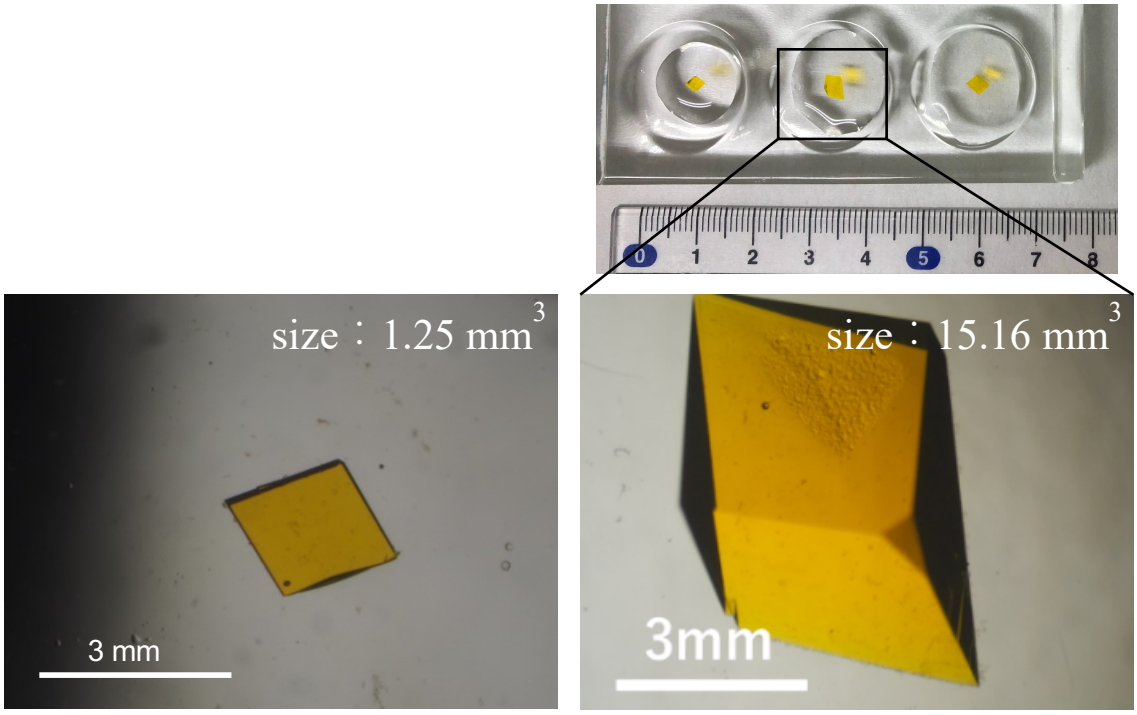

Figure 12. Picture of large crystals obtained.

Cryoprotection of Large Crystals

Large crystals obtained *via* the scaled-up batch method were carefully transferred into 300 µL of the stabilization buffer (0.24 M MES, 15% PEG 2000 in D_2O) in a hollow glass container using a pipetman fitted with a cut-tip to avoid direct contact with the crystals. Half of the mother liquor was removed, and an equal volume of 1% cryoprotectant solution (0.24 M MES, 15% PEG 2000, and 1% glycerol) was added. The solution was mixed thoroughly with gentle pipetting to ensure the crystal remained in the less concentrated layer, followed by a 10-minute incubation. The glycerol concentration was initially set at 1% and increased by 1% every 10 minutes until reaching 20%. The equilibrated crystal was then carefully picked up using a loop fashioned from surgical suture thread (Bear Medic Co., 40BA06-10), and flash-frozen in liquid nitrogen. To prevent the solution

from drying during the soaking process, the hollow glass container was sealed with a glass cover plate (4 × 3 cm) previously used for the sandwich crystallization method, with silicone grease (Toray Industries, Inc.) applied to the rim for a tight seal. All steps were conducted at a controlled temperature of 20 °C to ensure consistent conditions throughout the procedure.

Preparation of a Large Crystal of $wtFNR_{red}$ for Neutron Crystallography

The treatment for cryoprotection was performed in nearly the same manner as for the oxidized crystals. The only difference was that the cryoprotectant solution contained 5 mM dithionite. All steps described in this section were performed in an anaerobic chamber. All liquids and crystallization drop containing R-FNR crystals were stored under anaerobic conditions for one day prior to starting the experiment. A large $wtFNR_{oxi}$ crystal (~3 × 2 × 1 mm^3) was soaked in 100 μL of a dithionite-containing buffer (5 mM sodium dithionite, 0.2 M MES, pD 6.41, and glycerol). The glycerol concentration was initially set to 0% and was increased by 1% every 10 minutes until reaching 20%. At the 20% glycerol step, the crystals were soaked in the solution for an extended period, with a total soaking time of 5–6 hours in the dithionite-containing buffer. To keep the temperature constant, the samples were left in a 20°C incubator inside the anaerobic chamber, except when exchanging the buffer. After then, the equilibrated crystal was then carefully picked up using a loop fashioned from surgical suture thread (Bear Medic Co., 40BA06-10) or a thin nylon loop (ø 3.0 mm), and flash-frozen in liquid nitrogen. The absorption spectrum from the edge of large $wtFNR_{red}$ crystal mounted on the cryo-loop was measured using an offline micro-spectrophotometer at SPring-8/RIKEN, equipped with a DT-Mini and SD2000 (Ocean Optics Inc.).

Neutron Diffraction Experiments

Time-of-flight neutron diffraction data for oxidized and reduced R-FNR crystals were collected using the BL03 IBARAKI Biological Crystal Diffractometer (iBIX) at the Materials and Life Science Experimental Facility (MLF) of the Japan Proton Accelerator Research Complex (J-PARC) (36–38). The instrument was equipped with 34 two-dimensional position-sensitive detectors utilizing a scintillator sheet and wavelength-shifting fiber. (39) (**Figure 13**). The 2θ values for each detector are shown in **Table 3**. Data collection was conducted at 100 K. Both oxidized and reduced crystals were measured under the same conditions. The accelerator power of the proton beam for the spallation neutron source was 730 kW. A total of 24 datasets were collected using a circular beam with a diameter of 3 mm and a selected neutron wavelength range of 2.05–5.38 Å. Data reduction was performed using STARGazer 3.8.2 (40, 41), which employs the Elliptical Col method for peak integration (42). I determined the resolution limit of 1.8 Å based on the visual inspection of the resultant density maps together with the $I/\sigma(I)$ values in the highest resolution shell, completeness, and redundancy values.

Table 3. 2θ values for each detector in iBIX (from Prof. Kusaka)

	DetNo.	rrx	rry	2 θ
0 layer	1	0	−33	33
	25	0	−54	54
	34	0	54	54
	27	0	75	75
	26	0	−96	−96
	28	0	−117	117
	29	0	−139	139
	30	0	−161	161
+1 layer	24	−20.3	−24	31.04
	32	−20.3	24	31.04
	11	−20.3	−48	51.13
	33	−20.3	48	51.13
	3	−20.3	−72	73.15
	4	−20.3	−96	95.63
	5	−20.3	−120	117.97
	6	−20.3	−144	139.36
	9	−20.3	−168	156.55

	DetNo.	rrx	rry	2 θ
−1 layer	8	20.3	0	20.3
	7	20.3	−24	31.04
	10	20.3	−48	51.13
	2	20.3	−72	73.15
	12	20.3	−96	95.63
	13	20.3	−120	117.97
	31	20.3	−144	139.36
+2 layer	18	−40.9	−33	50.66
	19	−40.9	−66	72.1
	20	−40.9	−99	96.79
	21	−40.9	−132	120.38
	22	−40.9	−164	136.6
−2 layer	14	40.9	−99	96.79
	23	40.9	−132	120.38

	DetNo.	rrx	rry	2 θ
+3 layer	15	−62.3	−60	76.56
	16	−62.3	−120	103.44
	17	−62.3	−180	117.7

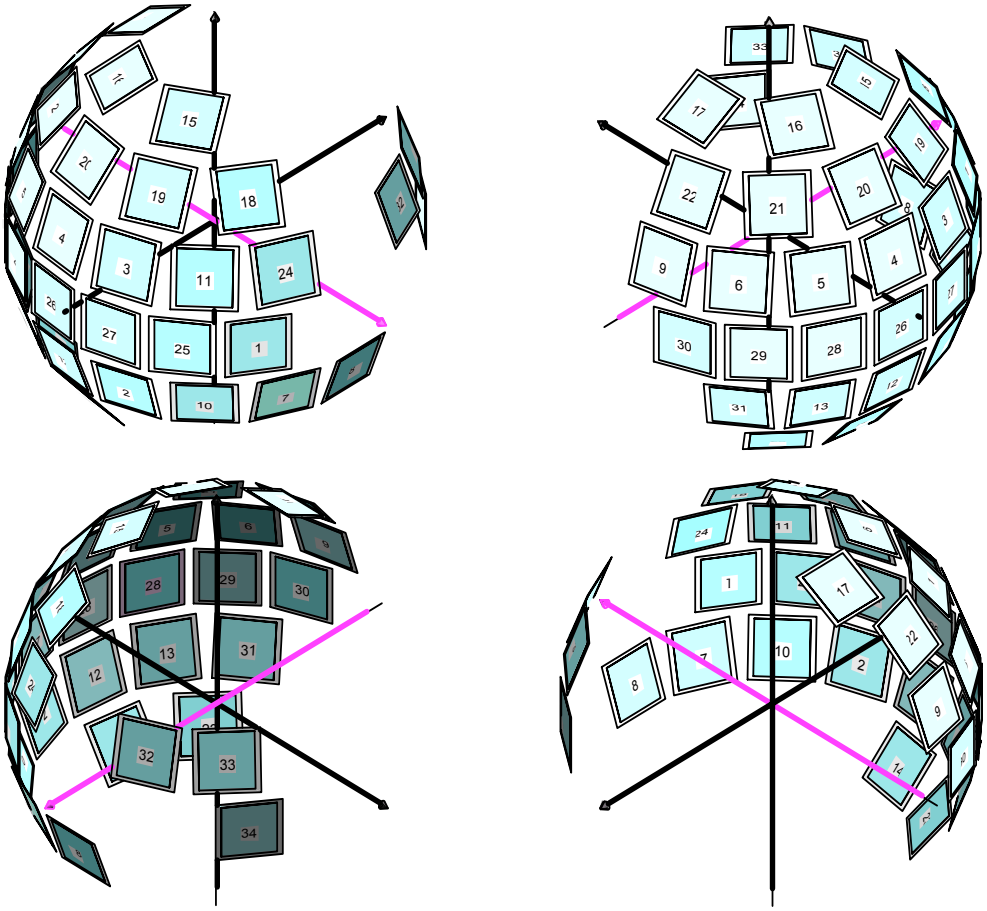

Figure 13. iBIX detector layout and numbers (from Prof. Kusaka)

Structure Refinements

Crystallographic refinement was performed using Refmac (43, 44) and COOT (34), utilizing only the neutron diffraction data and referencing the high-resolution X-ray structures obtained in this study (oxidized form: PDB ID 9KKG; reduced form: PDB ID 9KKH). The neutron diffraction dataset was converted to an MTZ file using ImportScaled in the CCP4 program suite (35). Five percent of the reflections were flagged as the Free R set. After several cycles of refinement, during which the model was modified in COOT, neutron scattering length density (NSLD) peaks, potentially corresponding

to hydrogen (H) and deuterium (D) atoms, were observed in the mF_o−DF_c NSLD difference map. H and D atoms were placed in the model using phenix.readyset. Exchangeable hydrogen sites were treated as disordered models with H and D atoms, and their initial occupancies were set to 0.5/0.5. Subsequently, exchangeable hydrogen atoms other than those in the main chains were removed from the atomic coordinates. H and D atoms at exchangeable sites in protein side chains, solvent water molecules, and ligands were manually added to the atomic coordinates and refined. H and D atoms were included in the model when corresponding peaks were observed in the mF_o−DF_c NSLD difference map. This process of modeling and refinement was repeated until all observable H and D atoms were included in the model. All polar hydrogens were treated as H/D exchangeable hydrogens, and their deuterium fractions were refined individually. The positions of all hydrogen and deuterium atoms were refined with restraints based on the monomer library in CCP4 (35).

3-3 Results

Spectral Measurement of Large Reduced Crystals

The results of microspectroscopic measurements performed on large crystals reduced through dithionite soaking are shown in Figure 14. Measurements were conducted on crystals with volumes ranging from 1 to 4 mm^3, and all crystals exhibited a single peak around 420 nm.

Neutron Diffraction Experiment

After purification, H/D exchange was conducted by replacing the standard buffer with a deuterated buffer. Crystals were then grown using solutions prepared with deuterated water and deuterated chemicals. For the $wtFNR_{oxi}$, a large crystal with a volume of 5.76 mm^3 was grown aerobically and used for neutron data collection. To prepare $wtFNR_{red}$ crystals, another large $wtFNR_{oxi}$ crystal (volume: 1.98 mm^3) was soaked in a dithionite solution under anaerobic conditions (Figure 15). Both crystals belonged to the space group of $P3_221$, with no significant differences in lattice constants. The resolution limit for neutron diffraction data was 1.80 Å for both oxidized and reduced crystals (Table 4). Refinement was performed exclusively using neutron structure factors due to the relatively high resolution of the neutron data. To ensure the accuracy of the structure, I used the high-resolution X-ray coordinates of carbon, nitrogen, oxygen, sulfur and phosphate atoms obtained in this study as a reference model and refined the structure by applying restraints on interatomic distances. The final neutron structure of $wtFNR_{oxi}$ included 3,234 hydrogen (H) atoms, 1,440 deuterium (D) atoms, and 446 deuterated water molecules. Similarly, the neutron structure of $wtFNR_{red}$ contained 3,096 H atoms, 1,367 D atoms, and 411 deuterated water molecules.

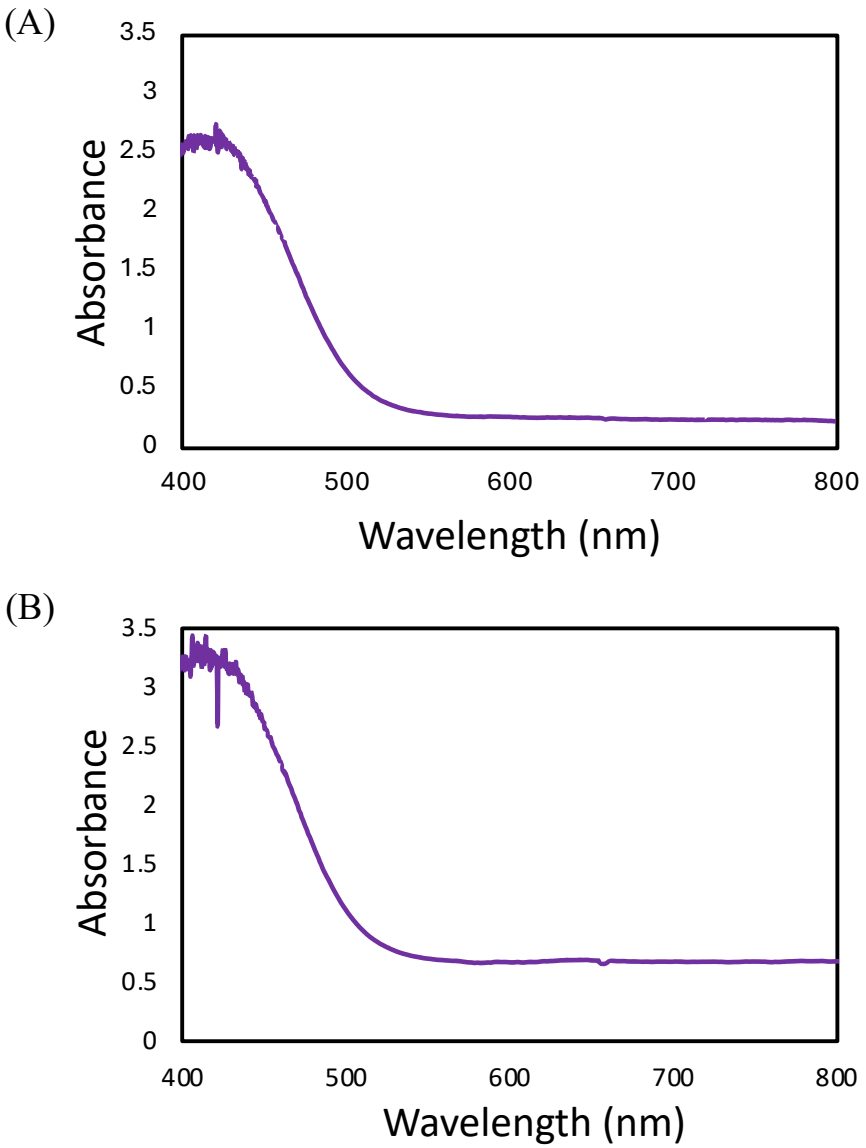

Figure 14. Absorption spectra of the large R-FNR crystals for neutron diffraction experiment by micro-spectrophotometry. Ultraviolet region (<400 nm) was not shown due to the high absorbance from added dithionite. (A) The crystal with a volume of 2.13 mm^3 (B) The crystal with a volume of 4.05 mm^3

Table 4. Crystallographic data and refinement statistics for neutron structures

	Neutron Oxidized form	Neutron Reduced form
Data-collection statistics		
Beamline	J-PARC MLF BL03	J-PARC MLF BL03
Wavelength (Å)	2.05-5.38	2.05-5.38
Space group	$P3_221$	$P3_221$
Unit cell *a, b, c* (Å) α, β, γ (°)	59.29, 59.29, 187.22, 90, 90, 120	59.32, 59.32, 187.69, 90, 90, 120
Temperature (K)	100	100
Resolution (Å)	19.41-1.80 (1.86-1.80)[1]	19.42-1.80 (1.86-1.80)[1]
Total reflections	327068 (25378)[1]	346849 (27228)[1]
Unique reflections	36250 (3539)[1]	36398 (3565)[1]
R_{merge}	0.4419 (1.8256)[1]	0.4940 (1.9039)[1]
R_{pim}	0.1548 (0.7180)[1]	0.1669 (0.7279)[1]
$CC_{1/2}$	0.9682 (0.3492)[1]	0.9613 (0.3668)[1]
Mean $I/\sigma(I)$	6.34 (1.04)[1]	5.41 (1.04)[1]
Completeness (%)	99.5 (99.5)[1]	99.9 (99.9)[1]
Redundancy	9.0226 (7.1710)[1]	9.5293 (7.6376)[1]
Refinement		
Resolution (Å)	19.415-1.80	19.425-1.80
No. of reflections	34484	34626
R_{work}	0.1905	0.1968
R_{free}	0.2430	0.2471
No. of atoms		
Total	6578	6361
Water	447	413
R.m.s.d. from ideal geometry		
Bond lengths (Å)	0.0079	0.0088
Bond angles (°)	1.6659	1.8197
PDB code	9KKC	9KK7

[1] Statistics in parentheses represent values calculated from the highest resolution shell.

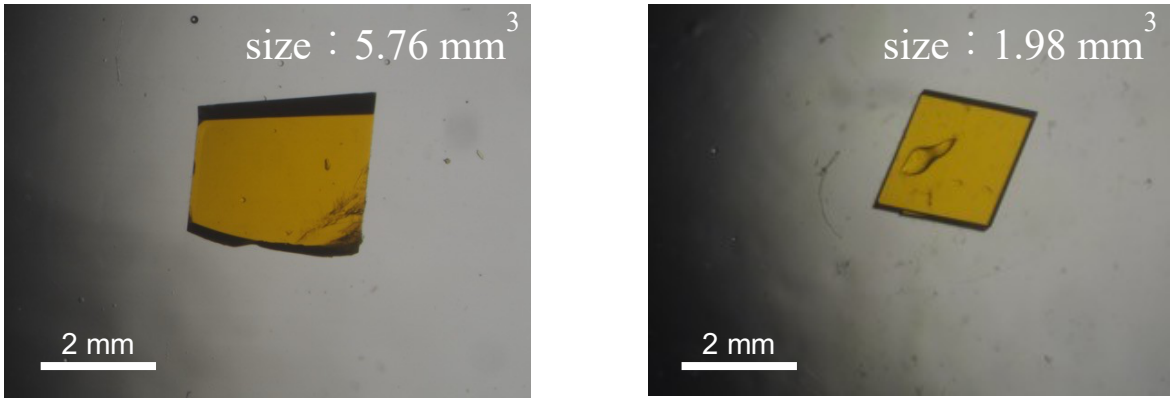

Figure 15. Large crystals used for neutron crystallography. The oxidized crystal is shown on the left, and the reduced crystal is shown on the right.

H/D substitution ratio of amide proton in main chain

In neutron crystallography, which involves the deuterium exchange of protein samples, makes it possible to observe solvent exposure and protein dynamics by analyzing the hydrogen-to-deuterium (H/D) substitution ratio. By focusing on the H/D substitution ratio of main-chain amide hydrogens, I identified the locations of residues with high and low deuterium occupancy (D fraction) within the structures (Figures 16). In β-sheets, residues with low D fractions were relatively abundant, likely reflecting the strong hydrogen bonds between β-strands. For α-helices, residues located within the protein core exhibited low D fractions, while those on the outer surface showed higher D fractions. This trend likely reflects differences in solvent accessibility, with residues on the outer surface being more exposed to solvent. Similarly, loop regions tended to have higher D fractions, consistent with their greater solvent exposure and flexibility. When comparing the H/D substitution ration between the oxidized and reduced states, I observed almost no significant differences. This suggests that the oxidized and reduced states have comparable structural stability, and that reduction does not cause major changes in the flexibility of the main-chain backbone. These results align with the findings from X-ray crystallographic analyses, which also

showed minimal differences in the backbone structure between the oxidized and reduced states.

Comparison of X-ray and Neutron Structures

The X-ray and neutron structures of both oxidized and reduced FNR were superimposed, ensuring that the positions of heavy atoms (C, N, O, S, and P) aligned well. This alignment was expected, as the X-ray structures served as the reference models for neutron refinement. Focusing on the $FADH_2$ in $wtFNR_{red}$, the position of the $FADH_2$ in the neutron structure closely matched that of conformation A in the X-ray structure (**Figure 17**). This observation suggests that $FADH_2$ predominantly exists in conformation A, while conformation B observed in the X-ray structure may represent an alternate state during the catalytic cycle. The non-observation of conformation B in the reduced neutron structure was due to the lower d-min compared to the X-ray. During refinement, water molecules in the neutron structure were not restrained to match those in the X-ray structures. This allowed for an independent assessment of water molecule positions, particularly those within 5 Å of the FAD/$FADH_2$ moiety (**Figure 17**). The X-ray structures revealed six additional water molecules compared to the neutron structures, likely due to the higher resolution limit of the X-ray data. Importantly, all water molecules identified by neutron crystallography were also present in the X-ray models, confirming their structural relevance.

Protonation State of the Isoalloxazine Ring of FAD and $FADH_2$

The protonation state of the isoalloxazine ring in $wtFNR_{oxi}$ and $wtFNR_{red}$ was analyzed using neutron crystallography. Differences between the oxidized and reduced structures were clearly visualized through F_o–F_c neutron omit maps, where hydrogen atoms of FAD/$FADH_2$ were excluded during map calculation (**Figure 18**). In the $wtFNR_{oxi}$ structure, no positive

peaks corresponding to deuterium were observed around the N1 and N5 atoms of the isoalloxazine ring (**Figure 18, upper**), indicating that FAD exists in the fully oxidized state. In contrast, the wtFNR$_{red}$ structure displayed two additional positive peaks derived from deuterium near the N1 and N5 nitrogen atoms, signifying that the FAD was reduced to $FADH_2$ (**Figure 18, lower**). The deuterium (D) fractions at these sites, DN1 and DN5, were calculated to be 0.64 and 0.96, respectively. The lower D fraction at DN1 suggests that the second reduction step, involving the protonation of the N1 nitrogen, may be incomplete in the crystalline state. The distinct D fractions at DN1 and DN5 highlight potential differences in the reduction environment or dynamics within the crystal.

DN1 and DN5 appeared in a non-planar fasshion

Also, intriguing finding was the bonding angles of DN1 and DN5 relative to the planar isoalloxazine ring. The angle from the plane was 5.53° for DN1 and 9.76° for DN5 (**Figure 19, lower**).

Calculate two angles: θ_{DN1}, the angle between Bond DN1-N1 and Plane C2-N1-C10; θ_{DN5}, the angle between Bond DN5-N5 and Plane C4X-N5-C5X. The names and positions of the atoms used in the calculation are shown in **Figure 19, upper**.

First, obtain two plane equations as below:

(1) Plane equation of C2-N1-C10:

$$-0.131x + 0.92y - 1.29z + 42.061 = 0$$

(2) Plane equation of C4X-N5-C5X:

$$0.339x - 0.856y + 1.336z - 43.328=0$$

Next, calculate the distance from DN1/DN5 to their corresponding plane: d_{DN1} = 0.0967Å and d_{DN5} = 0.167Å.

Then, use the bond length of DN1-N1and DN5-N5 to calculate the sine of the two angles, and finally we get θ_{DN1} = 5.53° and θ_{DN5} = 9.76°

(A)

```
FNR_oxi .........SK VSVAPLHLES AKEPPLNTYK PKEPFTATIV SVESLVGPKA PGETCHIVID 60
FNR_red .........SK VSVAPLHLES AKEPPLNTYK PKEPFTATIV SVESLVGPKA PGETCHIVID 60

FNR_oxi HGGNVPYWEG QSYGVIPPGE NPKKPGAPQN VRLYSIASTR YGDNFDGRTG SLCVRRAVYY 120
FNR_red HGGNVPYWEG QSYGVIPPGE NPKKPGAPQN VRLYSIASTR YGDNFDGRTG SLCVRRAVYY 120

FNR_oxi DPETGKEDPS KNGVCSNFLC NSKPGDKIQL TGPSGKIMLL PEEDPNATHI MIATGTGVAP 180
FNR_red DPETGKEDPS KNGVCSNFLC NSKPGDKIQL TGPSGKIMLL PEEDPNATHI MIATGTGVAP 180

FNR_oxi FRGYLRRMFM EDVPNYRFGG LAWLFLGVAN SDSLLYDEEF TSYLKQYPDN FRYDKVLSRE 240
FNR_red FRGYLRRMFM EDVPNYRFGG LAWLFLGVAN SDSLLYDEEF TSYLKQYPDN FRYDKVLSRE 240

FNR_oxi QKNRSGGKMY VQDKIEEYSD EIFKLLDGGA HIYFCGLKGM MPGIQDTLKK VAERRGESWD 300
FNR_red QKNRSGGKMY VQDKIEEYSD EIFKLLDGGA HIYFCGLKGM MPGIQDTLKK VAERRGESWD 300

FNR_oxi QKLAQLKKNK QWHVEVY 317
FNR_red QKLAQLKKNK QWHVEVY 317
```

(B)

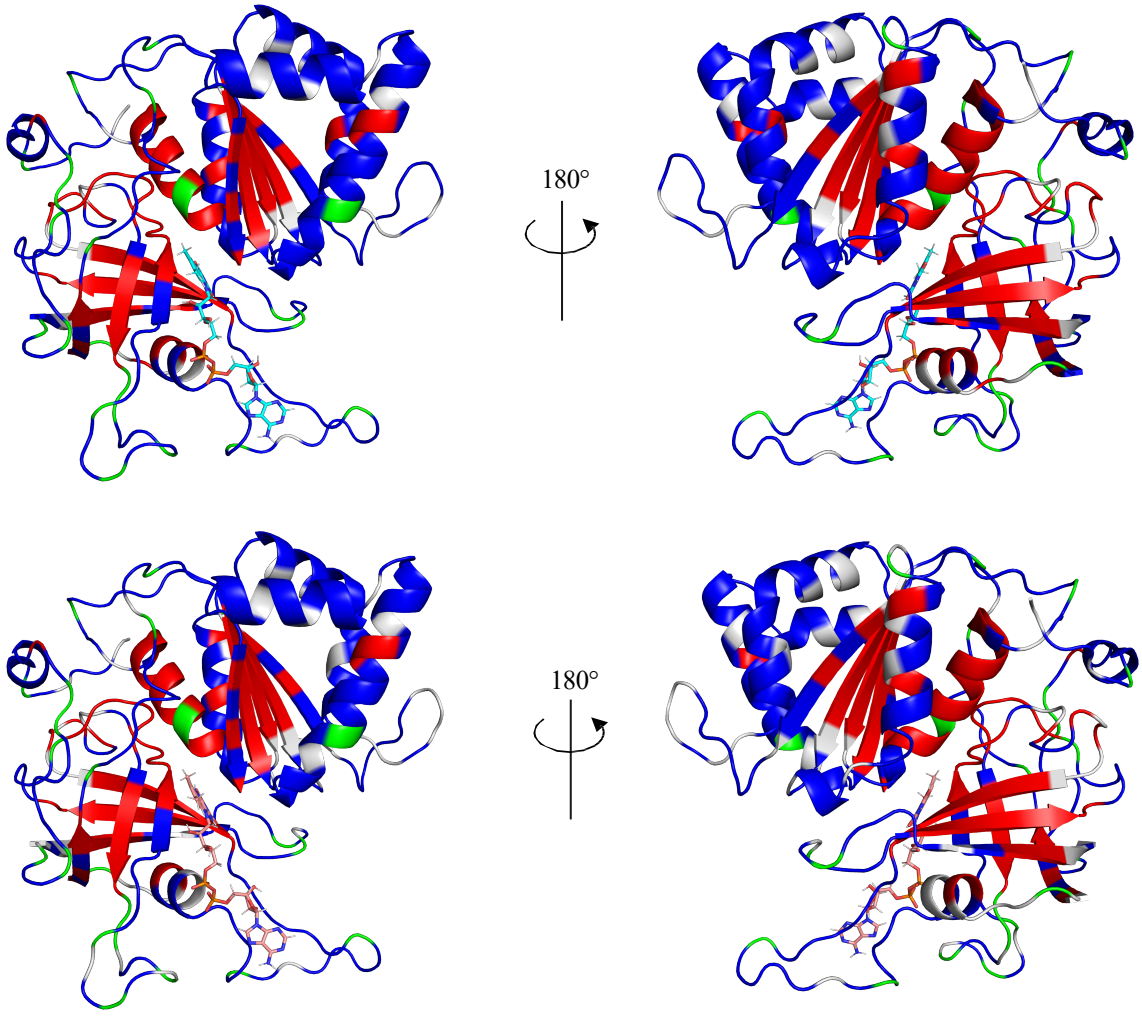

■ (D-fraction) ≧ 0.8　　□ 0.8 > (D-fraction) > 0.2

■ (D-fraction) ≦ 0.2　　■ Proline residue

Figure 16. Neutron Crystallography of wtFNRs (A) Comparison of the H/D substitution rates of amide protons for each residue in the sequence. Residues with a high H/D substitution rate (over 80%) are colored in blue, those with a low rate (under 20%) are colored red, and residues with intermediate rates are colored gray. Proline residues are shown in green. (B) Models color-coded based on the H/D substitution rate in the same color codes of panel B. The oxidized model is shown in the top, and the reduced model is shown in the bottom.

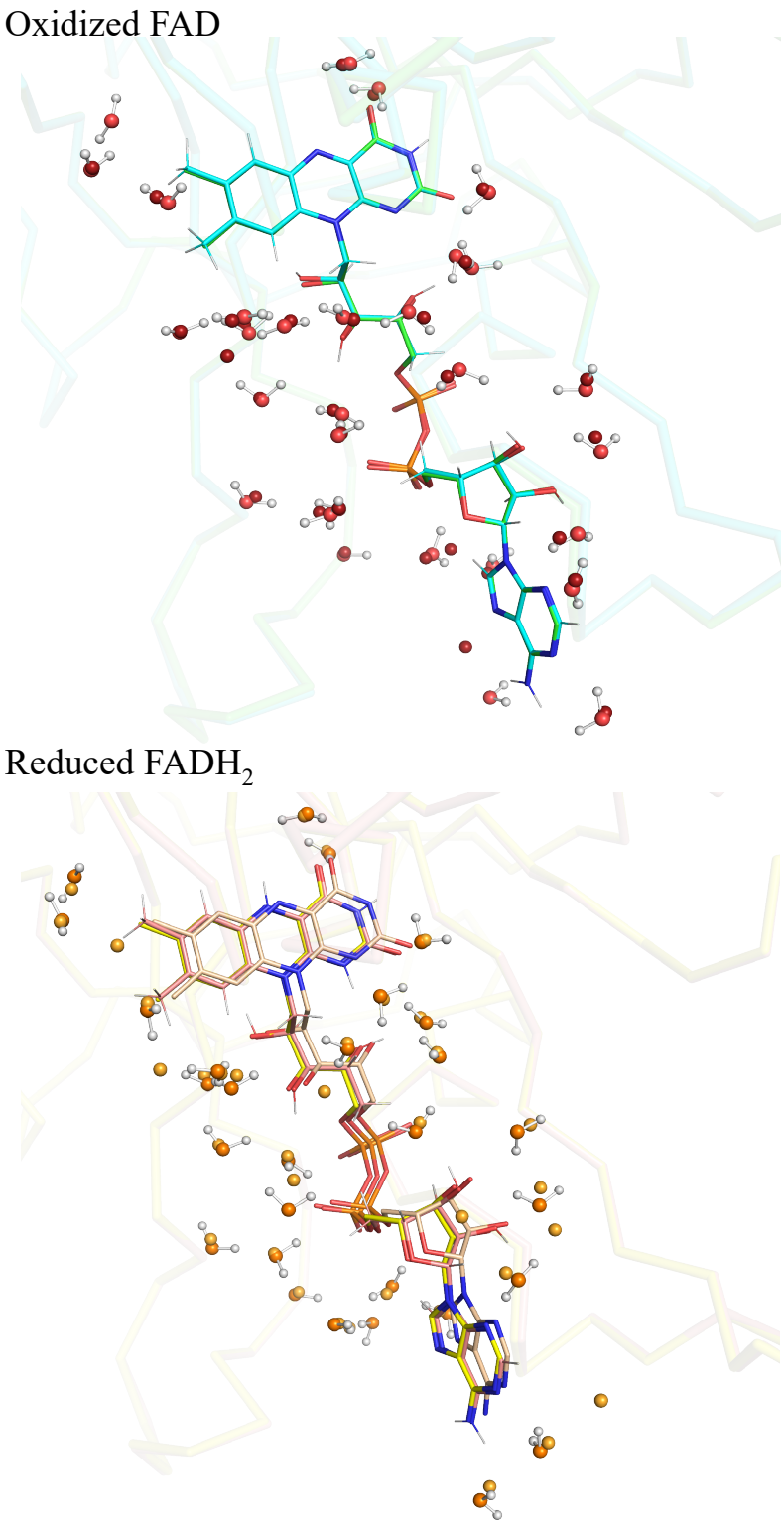

Figure 17. Comparison of X-ray and neutron structures around FAD/FADH$_2$: (Upper panel) Oxidized form: X-ray structure (model: green, water: dark red) and neutron structure (model: cyan, oxygen atoms of water: red). Each model was aligned based on the positions of all Cα atoms (backbone r.m.s.d. = 0.102 Å). (Lower panel) Reduced form: X-ray structure (conformer A: yellow, conformer B: pale orange, water: light orange) and neutron structure (model: salmon pink, oxygen atoms of water: orange). Each model was aligned based on the positions of all Cα atoms (backbone r.m.s.d. = 0.158 Å).

Oxidized FAD

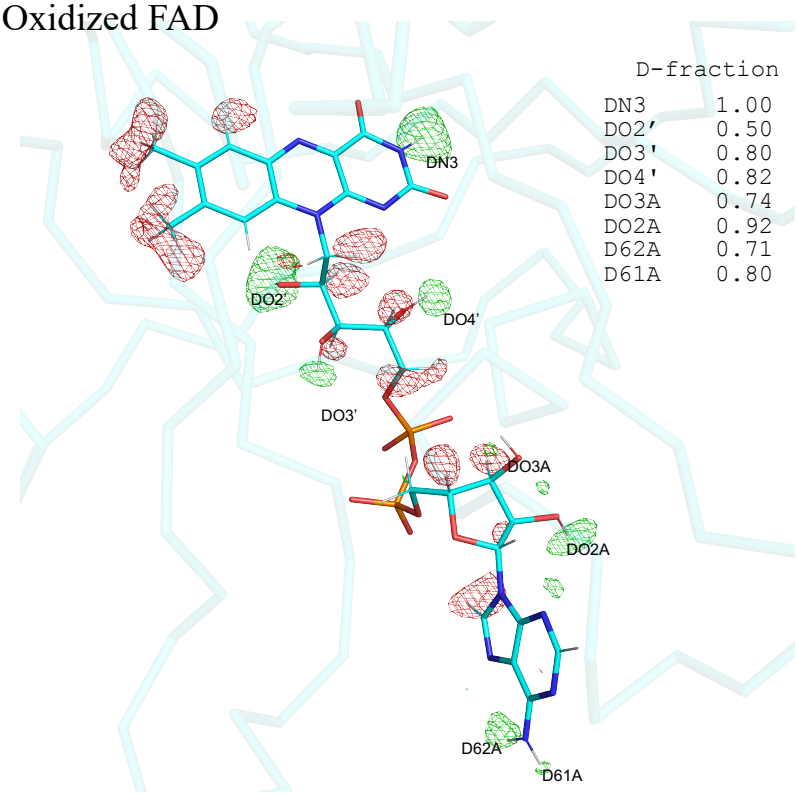

D-fraction	
DN3	1.00
DO2'	0.50
DO3'	0.80
DO4'	0.82
DO3A	0.74
DO2A	0.92
D62A	0.71
D61A	0.80

Reduced $FADH_2$

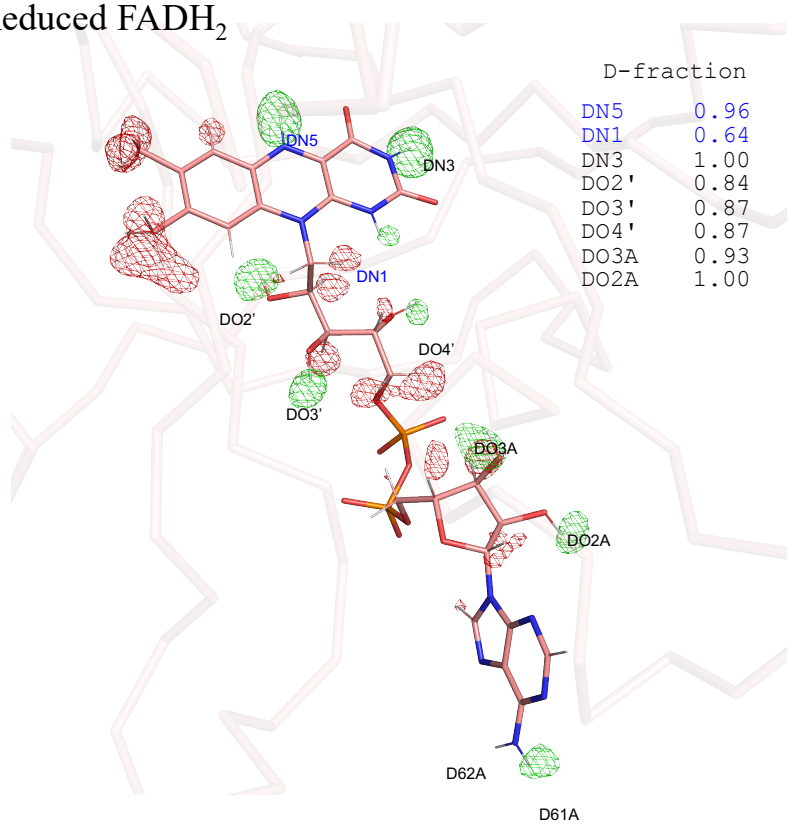

D-fraction	
DN5	0.96
DN1	0.64
DN3	1.00
DO2'	0.84
DO3'	0.87
DO4'	0.87
DO3A	0.93
DO2A	1.00

Figure 18. Neutron maps around FAD/FADH$_2$. The neutron F_o–F_c neutron omit scattering length density (SLD) map is contoured with positive (green) and negative (red) at +3.2σ and −3.2σ, respectively. The oxidized form is shown on the left, and the reduced form is shown on the right. D-fractions are also listed in the right corner.

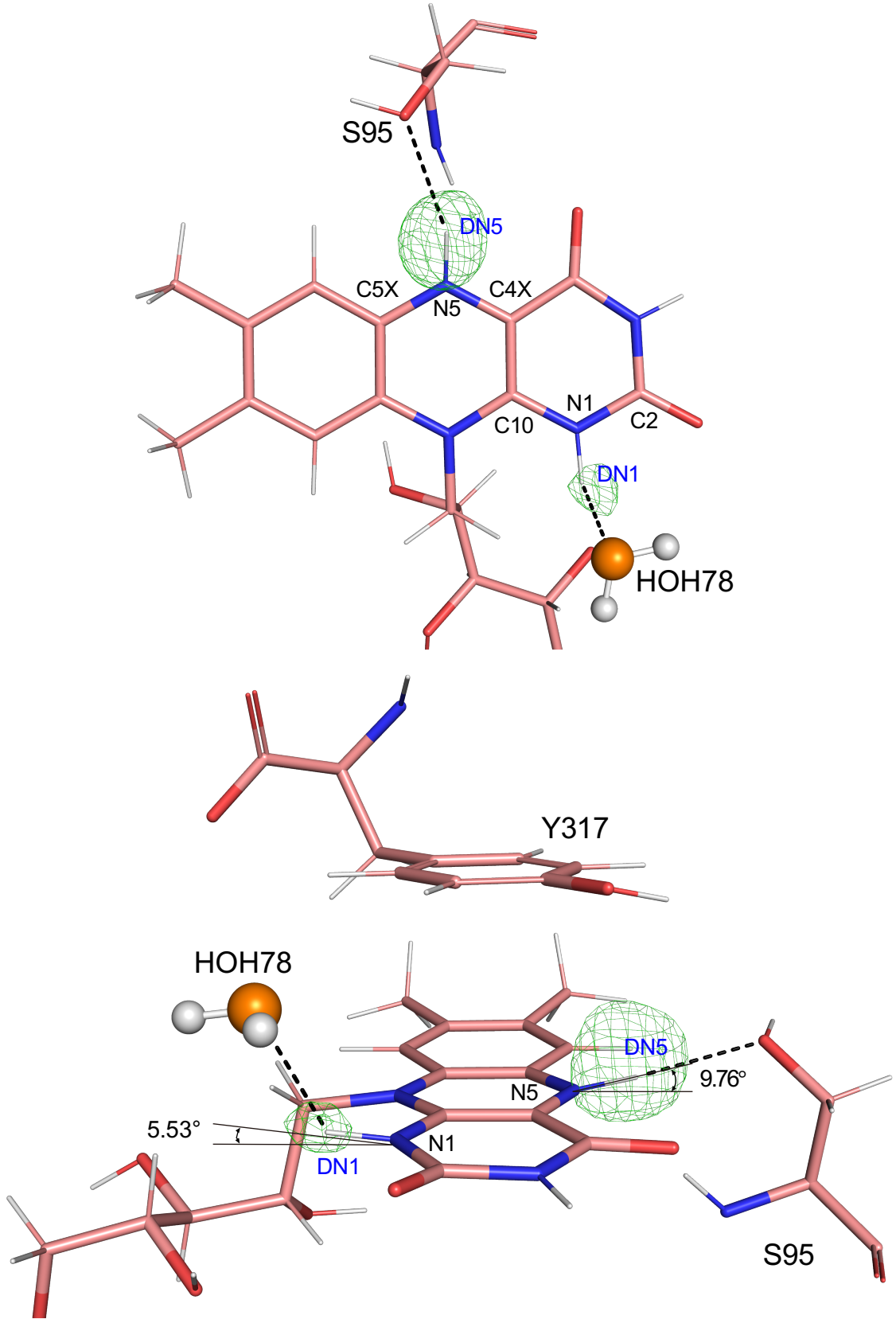

Figure 19. Enlarged view of the isoalloxazine ring in the reduced-state neutron structure. The neutron F_o–F_c neutron omit SLD map of deuterium atoms added during reduction is contoured with positive (green) at +3.2σ. Black dashed lines indicate hydrogen bonds. The lower panel shows the structure rotated by 90° along the x-axis and 90° along the y-axis.

3-4 Discussion

Two Non-Planar Hydrogen Atoms in $FADH_2$

In the reduced state, attention was focused on two deuterium atoms unique to this form. Peaks corresponding to these two deuterium atoms were observed at positions deviating from the plane of the isoalloxazine ring. Structurally, these hydrogen atoms would be expected to align with the plane; however, their tilted positions are likely caused by hydrogen bonds pulling them away. Specifically, these hydrogen bonds originated from the Oγ atom of Ser95 and the oxygen of HOH78, located above the isoalloxazine ring. The position of the isoalloxazine ring itself is stabilized by π-π interactions with Tyr317. However, the tilted hydrogen bonds from Ser95 and HOH78 introduce structural stress to the isoalloxazine ring, disrupting its planarity in the reduced state. This stress could potentially exert an upward force on Tyr317, which interacts with the ring via π-π stacking but needs to be away when $NADP^+$ would bind. Additionally, the increased flexibility of Tyr317 in the reduced state may facilitate structural rearrangements, allowing the nicotinamide ring of $NADP^+$ to be accommodated more easily. This combination of interactions and structural adjustments may play a critical role in the enzyme's function during the redox cycle.

Rearrangement of Hydrogen Bonds Through the Water Molecules Around

The neutron structures of $wtFNR_{oxi}$ and $wtFNR_{red}$ enabled clear visualization of hydrogen atoms in water molecules, allowing a detailed description of the hydrogen bond network in both redox states.

When the N1 atom is reduced and the HN1/DN1 atom is added, the hydrogen bond previously formed between the oxygen atom of HOH78 and the D1 atom of HOH60 in the oxidized state is disrupted. This results in a

switch in donor and acceptor roles, forming a new hydrogen bond between the HN1/DN1 atom and the oxygen atom of HOH78 (**Figure 20**). Additionally, the D1 atom of HOH60 rotates 180° in the opposite direction relative to the isoalloxazine ring, switching its donor and acceptor roles (H-O-H•••O to O•••H-O-H). This rotation creates a new hydrogen bond between the oxygen atom of HOH60 and the D1 atom of HOH78. In the oxidized state, the oxygen atom of HOH60 forms a hydrogen bond with the HE atom of the Arg115 side chain. Upon reduction, the reorganization of hydrogen bonds alters the orientation of HOH60, breaking this interaction. This structural rearrangement aligns with the changes observed in the Arg115 side chain in the reduced structure (**Figures 8 and 20**). These findings suggest that the reconfiguration of the hydrogen bond network accompanying the transition to the reduced state contributes to localized structural changes.

Upon single-step reduction, an HN5/DN5 atom binds to the N5 atom, forming a new hydrogen bond with the OG atom of Ser95 (**Figure 21**). This newly formed hydrogen bond pulls the side chain of Ser95 closer to the isoalloxazine ring. The OG atom of Ser95 was observed to move 0.32 Å closer to the isoalloxazine ring. Furthermore, the hydrogen bond network between Ser95 and Glu315, which is critical for electron transfer with Fd, is mediated by HOH197. Despite the positional shift of the Ser95 side chain upon reduction, the hydrogen bond network remains intact because HOH197 adjusts its orientation slightly to accommodate the change. At this point, the torsion angle involving the O atom and D2 atom of HOH196, along with the OG atom and HG atom of Ser95, changes from -129.48° in the oxidized state to -20.01° in the reduced state (**Figure 21**). These adjustments in the orientation of water molecules likely minimize structural changes in both the backbone and side chains, thereby preserving the overall structural integrity of the protein.

The changes in the hydrogen-bond network associated with redox changes, as revealed by the neutron structural analyses, are summarized, and illustrated in **Figure 22**. While the structural basis for the structural changes in Tyr317 and Arg115 upon reduction could not be explained by the X-ray structures alone, these changes can be rationalized by considering the hydrogen atom positions observed in the neutron structures. Upon reduction, the addition of a hydrogen atom to the N1 nitrogen atom of FAD triggers the formation of new hydrogen bonds between the surrounding water molecules and FAD(H_2). This, in turn, disrupts the interaction between the Arg115 side chain and HOH60, causing a positional shift in the Arg115 side chain. This explanation is consistent with the results observed in the difference maps from the X-ray structural comparisons. Furthermore, the addition of a hydrogen atom to the N1 nitrogen atom also leads to a positional shift of HOH27, which forms a hydrogen bond with the carboxyl group at the C-terminus of Tyr317. As a result, the carboxyl group of Tyr317 moves by 0.84 Å, providing an explanation for the structural changes observed in this region.

Proton Pathway with Reduction reaction

The mechanism by which the N5 atom of FAD receives a proton during reduction by ferredoxin remains unclear. However, previous studies have suggested several possible pathways. In this study, we considered the pathway through which the N5 atom acquires a proton, based on existing structural data and insights from earlier research. For the N5 atom to acquire a proton, it must be supplied from either the solvent or a nearby proton donor. However, in the crystal structure, the N5 atom is not solvent-exposed, and no direct proton donor has been identified. Regarding this issue, a previous study on spinach FNR (45) proposed two potential mechanisms.

1. Proton Supply *via* Ser95

Ser95 is conserved across almost all members of the FNR family and is considered a candidate proton donor. The hydroxyl group of the Ser95 side chain forms a hydrogen-bond network through Glu315 and HOH197, both of which are solvent-exposed, suggesting the possibility that Ser95 could acquire a proton from the side chain of Glu315. However, neutron structural analysis of the oxidized form of FNR showed no evidence of protonation at Glu315, as indicated by the absence of positive signals in the F_o-F_c neutron scattering length density map derived from deuterium. This result suggests that Glu315 is deprotonated in the oxidized state, indicating that Ser95 is not directly supplied with protons from Glu315. Therefore, the proton supply pathway *via* Glu315 is likely to be unfavorable.

2. Proton Supply *via* HOH27

HOH27 has been identified as a water molecule that could potentially accept exchangeable protons from the side chains of Tyr317 or Ser95. HOH27 is present at a corresponding position not only in spinach FNR but also in FNRs from maize, pea, and paprika, suggesting its functional importance due to its high conservation. On the other hand, in a similar redox enzyme, phthalate dioxygenase reductase (PDR), the corresponding water molecule is absent despite the presence of a nearby threonine residue (46). This difference supports the hypothesis that HOH27 plays a unique role in the proton transfer mechanism specific to FNR.

In this study, neutron structural analyses of both the oxidized and reduced states revealed that the D-fraction (deuterium substitution rate) of the phenolic hydrogen atom of Tyr317 was extremely high, at 0.96 in the oxidized state and 0.99 in the reduced state. These findings indicate that Tyr317 has a strong proton-donating capability and suggest that HOH27 plays a significant role in a proton transfer pathway mediated by Tyr317. The high D-fraction values further imply that Tyr317 remains actively involved

in proton transfer, regardless of the redox state of FNR. This evidence strongly supports the importance of HOH27 in the proton transfer process.

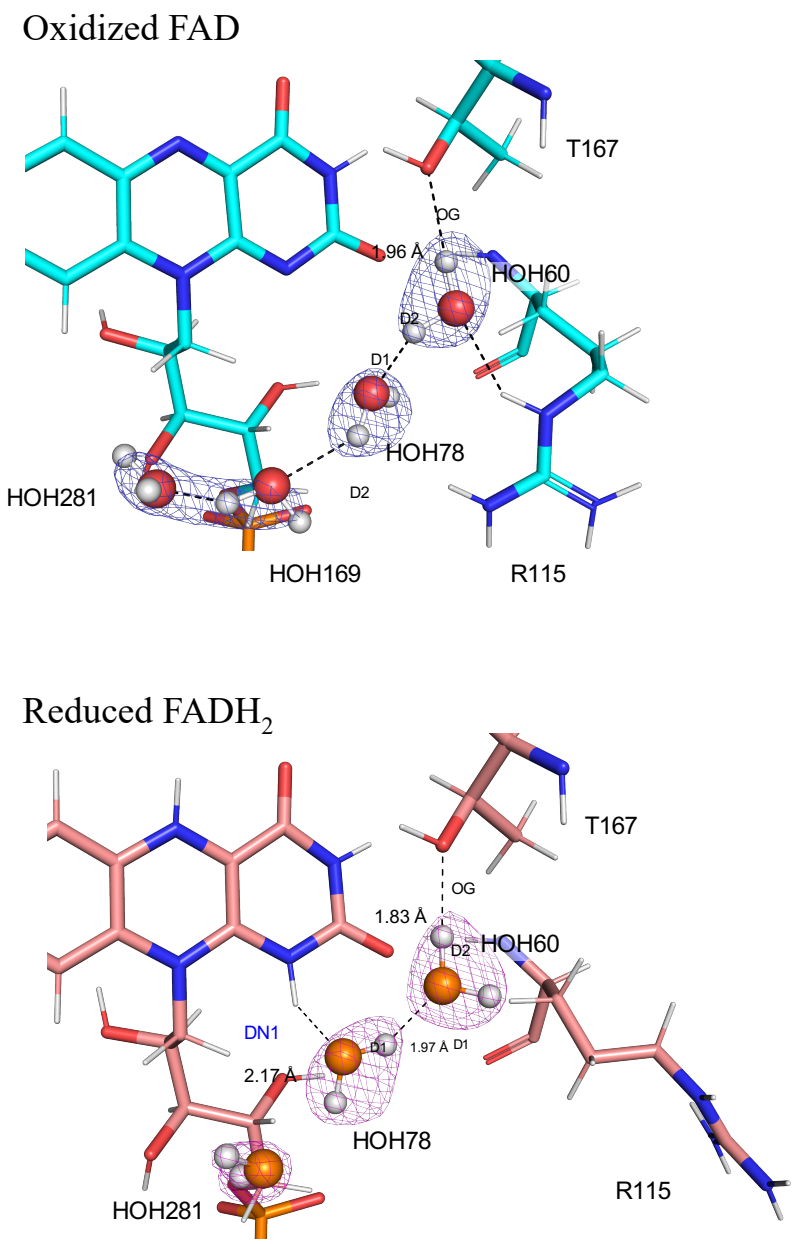

Figure 20. Comparison of the Hydrogen Bond Network Around FAD/FADH$_2$ Between Amino Acid Residues and Water Molecules. Hydrogen bond network focused on the DN1 atom. The neutron $2F_o–F_c$ neutron scattering length density (SLD) map is contoured at 1.8σ

Oxidized FAD

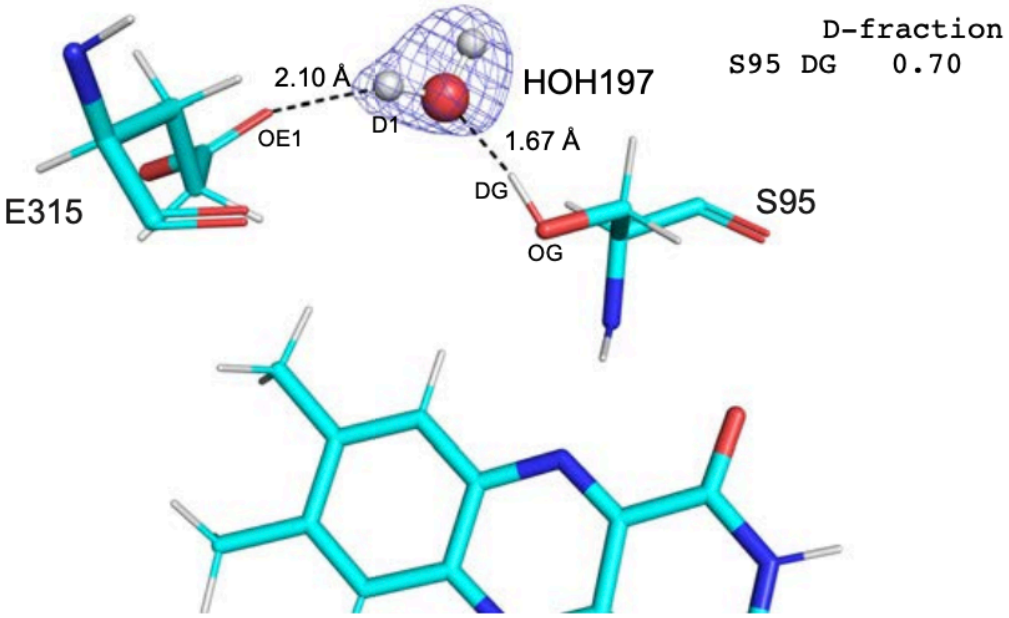

Reduced FADH、

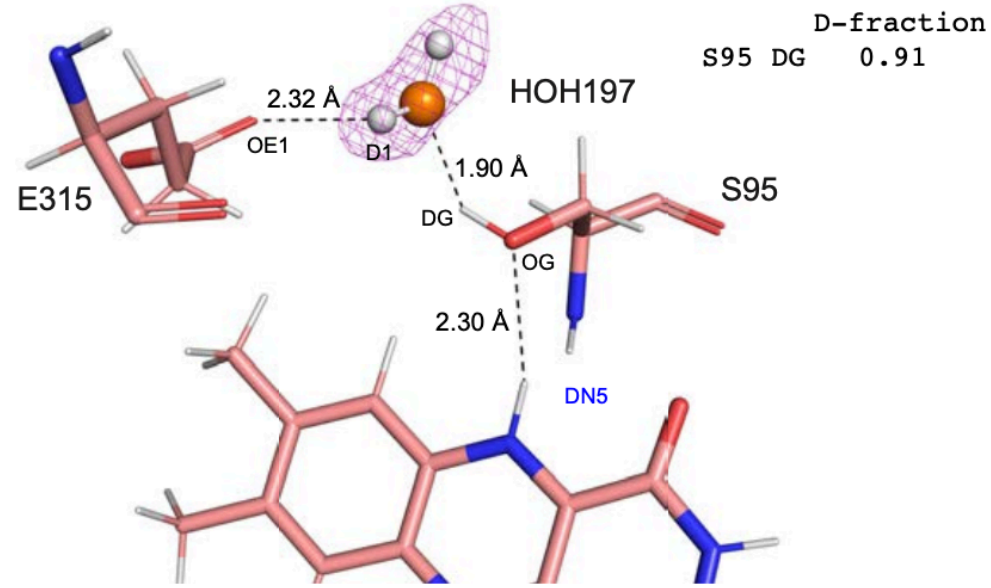

Figure 21. Comparison of the Hydrogen Bond Network Around FAD/FADH$_2$ Between Amino Acid Residues and Water Molecules. Hydrogen bond network focused on the DN5 atom. The neutron $2F_o–F_c$ neutron scattering length density (SLD) map is contoured at 1.8σ

Oxidized FAD

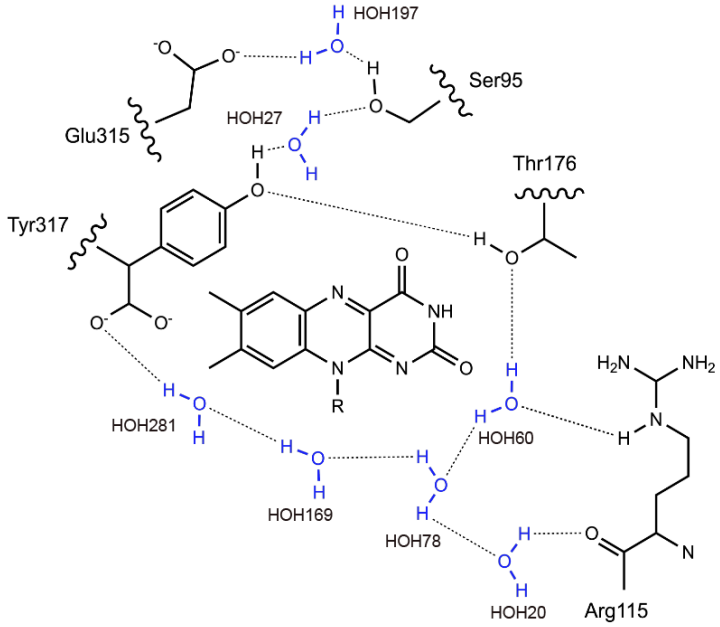

Reduced $FADH_2$

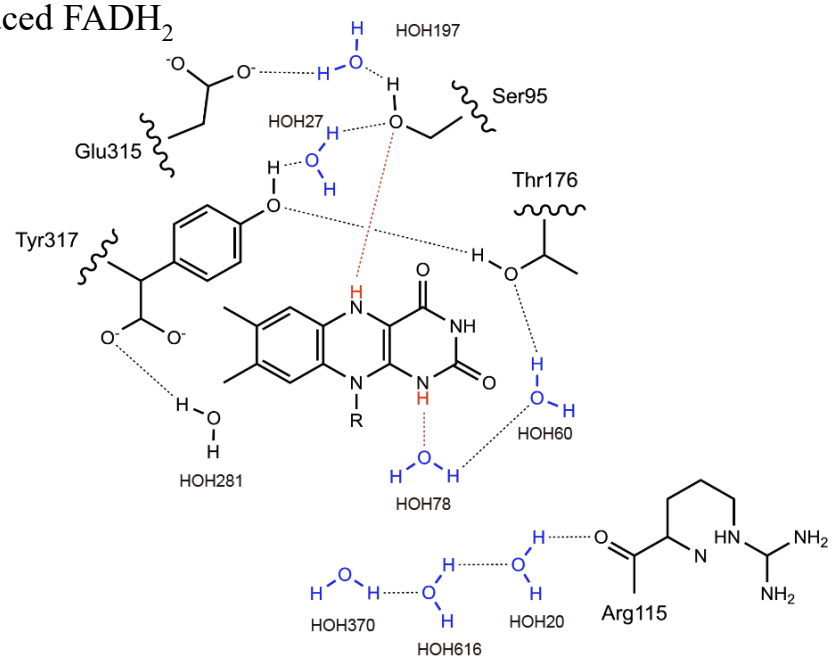

Figure 22. Proposed Redox-dependent Rearrangement of Hydrogen Bonds within FNR

The proposed reduction-induce rearrangement of hydrogen bonds is illustrated, highlighting important residues involved in the process.

IV. CONSIDERATIONS ON THE MECHANISMS OF REDOX DEPENDENT CONFORMATIONAL CHANGE OF FNR BASED ON OXIDIZED AND REDUCED STRUCTURES OF ITS MUTANT

4-1 General outline

In Chapter II, structural comparison of high-resolution structure of oxidized and reduced FNR, obtained with careful consideration of X-ray radiation damage, revealed subtle conformational changes around FAD induced by redox transitions. These changes included slight positional shifts of surrounding water molecules and amino acid side chains. However, the question remained as to how the addition of hydrogen atoms during reduction could induce such structural changes.

Subsequently, in Chapter III, neutron crystallographic analyses, which determined the positions of hydrogen atoms in the oxidized and reduced states, provided an explanation for the structural changes observed in the X-ray structures during redox transitions. Furthermore, a structural change in Arg115 was captured for the first time in this study, leading to the hypothesis that Arg115 influences the affinity between Fd and the enzyme. This hypothesis should be confirmed by determining the structures of Arg115 mutants. Notably, Arg115 is a residue unique to R-FNR, while its equivalent in L-FNR is Lys.

In this chapter, two mutants of R-FNR, R115A and R115K, were generated. For R115A, X-ray diffraction data were collected with consideration of X-ray irradiation damage, and the oxidized structure ($R115A_{oxi}$) was determined at 1.35 Å. Similarly, for R115K, X-ray diffraction data were

collected with consideration of X-ray irradiation damage, successfully determined the structures of the oxidized and reduced forms ($R115K_{oxi}$ and $R115K_{red}$) at 1.40 Å and 1.44 Å, respectively. Structural analysis of these mutants suggests that in root-type FNR, Arg115 serves as a structural determinant that induces significant differences in the interaction between Fd and FNR. Structural change of Arg115 is attributed to the redox-dependent of hydrogen bond network rearrangement involving water molecules surrounding FAD with reduction.

4-2 Material and methods

Preparation of plasmids

Plasmids of the mutants were created with polymerase chain reaction (PCR) method using PrimeSTAR® Max DNA polymerase (TAKARA BIO INC.) based on the plasmid of native R-FNR. The sequence of primers used for the PCR method was listed in **Table 5**.

The detailed method for PCR followed the standard protocol of PrimeSTAR® Max. 0.5 μL of forward primer (5 pmol/μL), 0.5 μL of reverse primer (5 pmol/μL), 1 μL of R-FNR plasmid (vector: pQE-60, 10 ng/μL) and 5 μL of 2×PrimeSTAR Max Premix (DNA polymerase) were mixed and filled with sterilized water up to 10 μL. PCR was performed by 30 cycles of 10 seconds of denaturation step (98 ºC), 15 seconds of annealing step (55 ºC) and 30 seconds of extension step (72 ºC). To remove the remaining template plasmids, 1 μL of Dpn1 (10 U/μL, TAKARA BIO INC.) and 1μL of 10×CutSmart were added to the 9 μL product of PCR and incubated for 1 hour under 37 ºC. Then, transformation was performed by adding 0.5 μL of the purified plasmid to 100 μL of competent cell of *E.coli* (DH5α and JM109) and heated with 45 ºC hotplate for 43 seconds. The transformed cell was diluted with 400 μL of SOC medium and performed recovery culture by shaking for one hour under 37 ºC. Then, 500 μL of the culture was expanded on agarose gel plate containing sterilized LB medium and Ampicillin Sodium (100 μg/mL). After overnight incubation under 37 ºC, some colonies were appeared on the plate. One of the colonies was added to 3 mL of sterilized LB medium containing Ampicillin Sodium (100 μg/mL) and shaken overnight under 37 ºC. From this culture, plasmid was purified using Miniprep DNA Purification Kit (TAKARA BIO INC.).

Table 5. The sequence of the primers used to synthesize plasmids of the mutants.

Primer name	Sequence (3'->5')	Tm
rFNR_R115A_pro	GTGTCGCCCGTGCAGTTTATTATGATCCTG	55
rFNR_R115A _ter	CTGCACGGGCGACACACAAGCTTCC	55
rFNR_R115K_pro	GTGTCAAACGTGCAGTTTATTATGATCCTG	55
rFNR_R115K_ter	CTGCACGTTTGACACACAAGCTTCC	56

The PCR products were transformed into *E.coli* DH5α and JM109, and the R115A and R115K mutation were confirmed by plasmid sequencing. Expression and purification of the mutants were carried out using the same protocol as for wtFNR. The R115A mutant crystal was obtained using the hanging drop vapor diffusion method. The protein stock was diluted to a concentration of 30 mg/mL in a buffer containing 50 mM Tris-HCl (pH 7.5) and 150 mM NaCl and mixed with an equal volume of precipitant solution (0.2 M MES, pH 6.0, and 26% PEG 2000). The mixture was equilibrated against the precipitant solution at 20 °C. After crystal growth was complete, single crystals (~200 × 300 × 100 μm³) were soaked in a cryoprotectant solution (20% glycerol, 0.24 M MES, pH 6.4, and 15% PEG 2000) for 10 seconds, mounted with a CryoLoops™ (Hampton Research), and cryocooled in liquid N2.

R115K mutant crystal was also obtained using the hanging drop vapor diffusion method same as R115A mutant. The protein stock was diluted to a concentration of 30 mg/mL in a buffer containing 50 mM Tris-HCl (pH 7.5) and 150 mM NaCl and mixed with an equal volume of precipitant solution (0.2 M MES, pH 6.0, and 25% PEG 2000). The mixture was equilibrated against the precipitant solution at 20 °C. After crystal growth was complete, single crystals (~200 × 300 × 100 μm³) were soaked in a cryoprotectant solution (20% glycerol, 0.24 M MES, pH 6.4, and 15% PEG 2000) for 10 seconds, mounted with a CryoLoops™, and cryocooled in liquid N2 following the same procedure as that used for the R115A mutant.

Crystallization of R115K mutants of reduced form

Neutron crystallography of reduced form results did not exclude the possibility that soaking the oxidized crystals in a buffer containing dithionite alone was insufficient for complete reduction. Therefore, to obtain fully reduced crystals, dithionite was added to the protein solution to a final concentration of 10 mM. The solution spectrum was then measured to confirm the reduced state of R-FNR. In the anaerobic chamber, dithionite was added to the oxidized R-FNR solution to a final concentration of 10 mM, followed by incubation at 20°C for 1 hour. Furthermore, the spectrum of 10 mM dithionite alone, measured under the same conditions, was subtracted to obtain the spectrum of the reduced state.

Then, crystallization was performed using this reduced R-FNR solution in an anaerobic chamber. Crystallization was carried out using the hanging-drop vapor diffusion method. For cryoprotection, the crystals were soaked for approximately 10 seconds in a cryoprotectant solution containing 10 mM dithionite, 20% glycerol, 0.24 M MES (pH 6.4), and 15% PEG 2000. The crystals were then frozen in liquid nitrogen using CryoLoops™, following the same procedure as for the wild-type protein.

Data collection and analysis for mutants

X-ray diffraction experiments for the oxidized mutant were conducted at BL44XU of SPring-8. An EIGER X 16M detector was used to detect diffraction spots. A focused X-ray beam (λ=0.9000 Å) was used for the diffraction experiment. The beam size was adjusted using a 30 μm pinhole, and the beam flux was attenuated with a 1.6 mm aluminium foil. To prevent X-ray radiation damage, data were collected in six non-overlapping points from a single crystal. X-ray data collection began at one end of the crystal. A total of 200 images covering 20° of rotation were collected from one

assigned point. Subsequently, the measurement point was moved 60 μm towards the opposite end, and another 20 images were collected from a fresh part of the crystal. This process of crystal movement and data collection was repeated until the entire angular range was covered by six assigned exposure points. All images were processed using XDS (30), and the six datasets were scaled and merged with XSCALE. Data collection statistics were calculated using AIMLESS (35). Phasing and model refinement were performed using the same procedure as for wtFNR.

4-3 Results

Preparation and crystallization of R-FNR mutants

Recombinant R-FNR mutants were successfully produced using a synthetic gene with altered codon usages optimized for expression in *E. coli*. The final purification step, gel filtration, R-FNR eluted as a single peak (**Figure 23**). R-FNR crystals used for X-ray data collections were reproducibly obtained by optimized crystallization conditions (**Figure 24**). Also, crystallization of the R115K mutant in reduced state was performed in an anaerobic chamber using reduced R115K solution, resulting in the formation of light yellow crystals (**Figure 25**).

Spectrum measurement in solution

The absorption spectra of the oxidized and reduced states in solution are shown in Figure 26. The peaks around 460 nm and 490 nm, derived from oxidized FAD, decreased, while a peak appeared around 420 nm, indicating that the mutant proteins were similarly reduced. In the oxidized state, no significant differences were observed between the wtFNR and the two mutants (R115A and R115K). However, in the reduced state, the 420 nm peak, which is characteristic of the hydroquinone form, exhibited a slight red shift in both mutants. A previous study reported theoretical absorption spectra reflecting redox states for plant cryptochromes containing FAD, based on QM/MM calculations (48). Comparison with these theoretical spectra suggests that the red shift in the 420 nm peak observed in the two mutants may indicate incomplete reduction of FAD, resulting in a mixture of $FADH^-$ and $FADH_2$ states. This finding further suggests that Arg115 may play a role in the electron transfer process during the reduction of FAD.

Data statistics and the overall structure

The structure of the R115Aoxi was determined at 1.35 Å and the structures of the R115Koxi and R115Kred were determined at 1.40 Å and 1.44 Å. Statistics for data collection, analysis and crystallographic refinement for $R115A_{oxi}$ is shown in **Table 6** and $R115K_{oxi}$ and $R115K_{red}$ are shown in **Table 7**. Their space group was $P3_221$ which was same as that of wtFNR, and there was no significant difference on the unit cell constants between mutants and wtFNR. The main chain structure of mutants were highly similar to those of $wtFNR_{oxi}$ and $wtFNR_{red}$. RMSDs between refined models of wtFNR and mutants were 0.191 Å for oxidized R115A, 0.173 Å for oxidized R115K, and 0.130 Å for reduced R115K according to the positions of the C α atoms. In the R115K mutants, as with wtFNR no significant structural changes were observed in the main chain skeleton upon reduction (backbone r.m.s.d.=0.089 Å).

Focusing on the water molecules surrounding FAD, the arrangement of water molecules in the $R115A_{oxi}$ structure closely resembled that of $wtFNR_{red}$ (**Figure 27**). Surprisingly, there were no significant changes in the arrangement of the water around FAD in $R115K_{oxi}$ and $R115K_{red}$. The arrangement of the water was similar to that of $wtFNR_{red}$ (**Figure 28**).

(A)

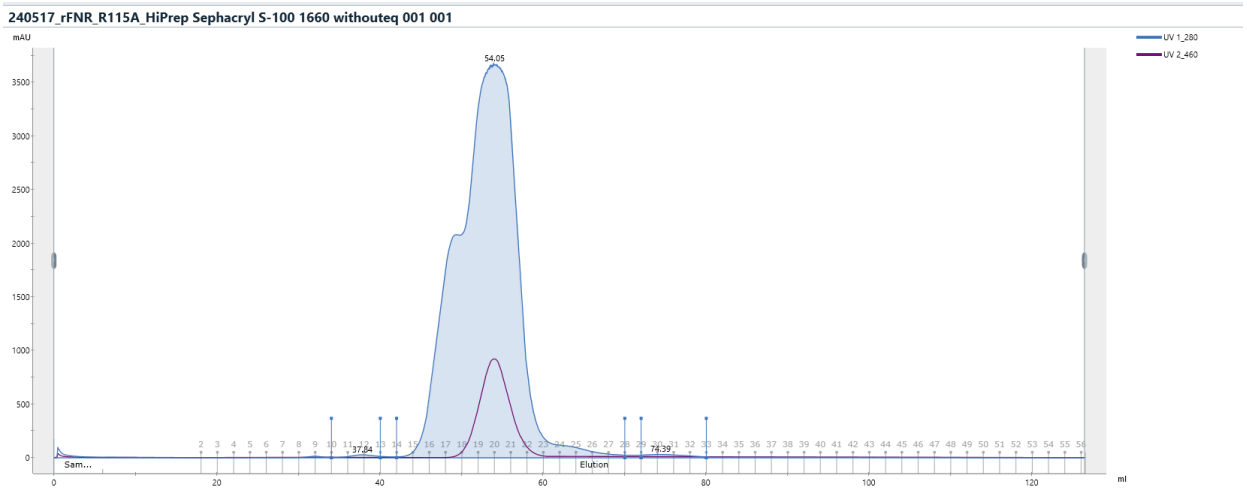

(B)

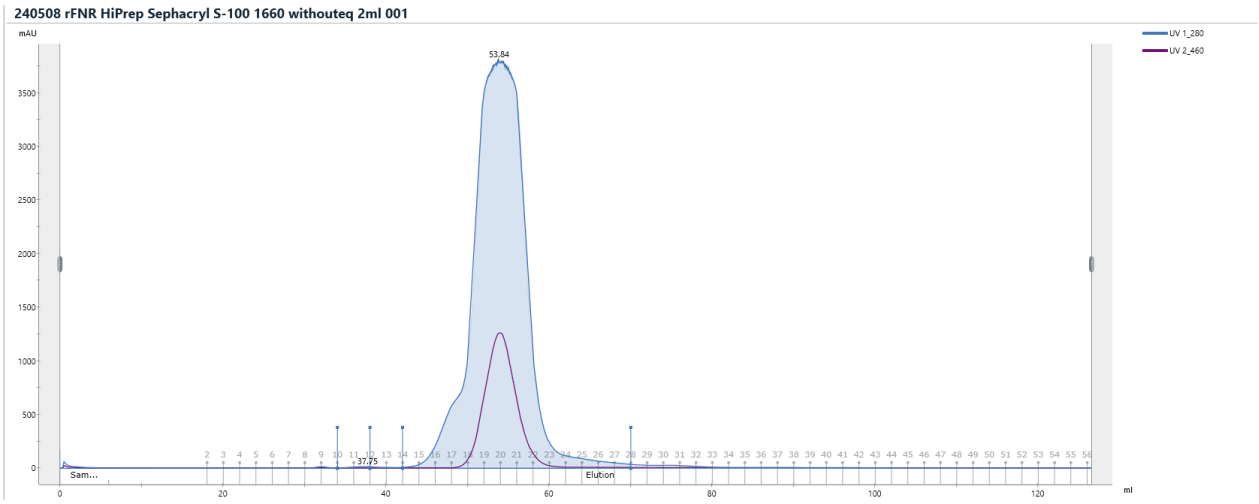

Figure 23. The absorption of elution of gel filtration of mt R-FNR at 280 (blue) and 460 (purple) nm. (A) R115A mutant, (B) R115K mutant.

(A)

Crystal composition	
mtFNR R115A	30 mg / mL
MES buffer (pH6.0)	0.2 M
PEG 2000	26%

(B)

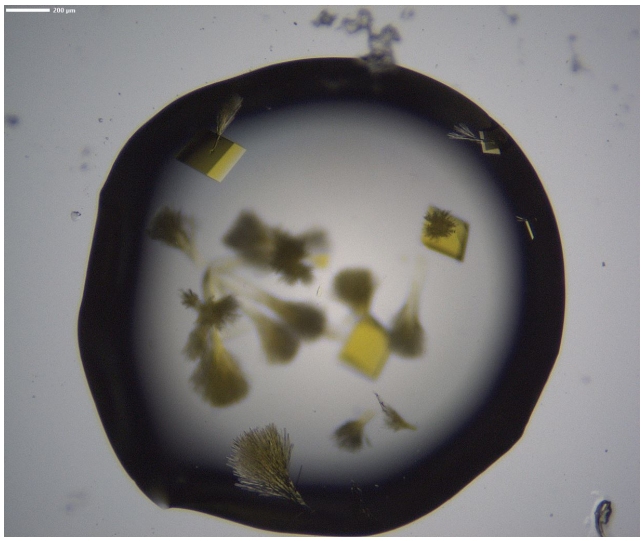

Crystal composition	
mtFNR R115K	30 mg / mL
MES buffer (pH6.0)	0.2 M
PEG 2000	25%

Figure 24. Crystals of mutants by vapor diffusion method by vapor diffusion method in oxidized state. (A) $R115A_{oxi}$, (B)$R115K_{oxi}$.

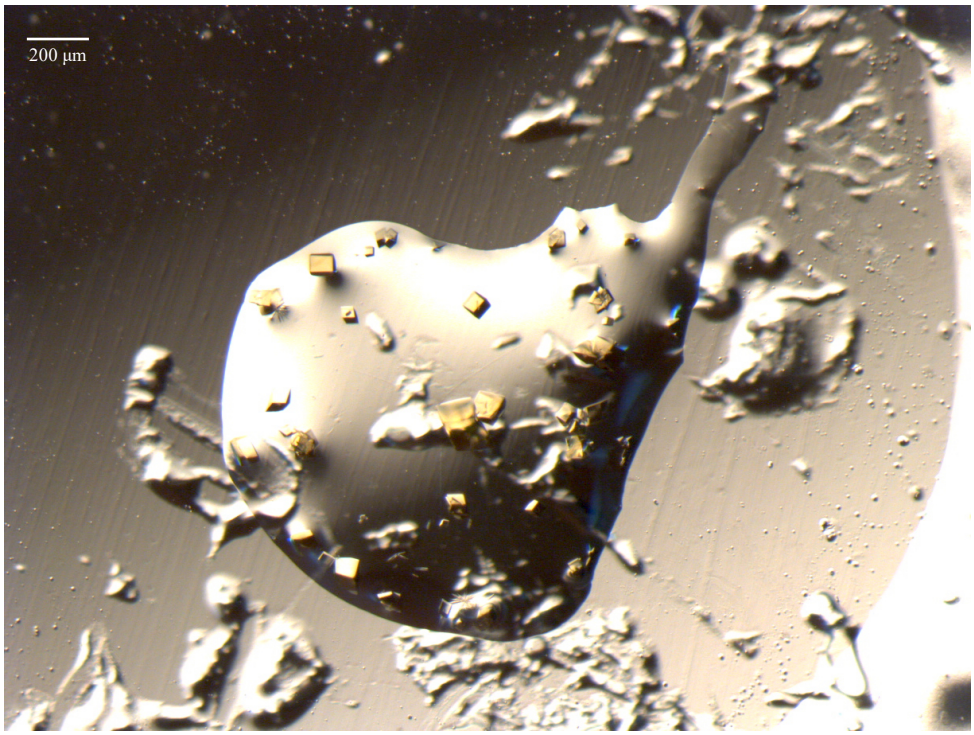

Crystal composition	
mtFNR R115K	27.02 mg / mL
MES buffer (pH6.0)	0.2 M
PEG 2000	25%

Figure 25. Crystals of R115K by vapor diffusion method by vapor diffusion method in reduced state at anerobic chamber.

Table. 6 Crystallographic data and refinement statistics of R115A mutant

	$R115A_{oxi}$
Data-collection statistics	
Beamline	SPring-8 BL44XU
Wavelength (Å)	0.90000
Space group	$P3_221$
Unit cell *a, b, c* (Å) α, β, γ (°)	59.17, 59.17, 186.18, 90, 90, 120
Temperature (K)	100
Resolution (Å)	49.41-1.35 (1.37-1.35)[1]
Total reflections	481133 (13676)[1]
Unique reflections	83861 (4086)[1]
R_{merge}	0.111 (0.607)[1]
R_{meas}	0.121 (0.721)[1]
R_{pim}	0.046 (0.384)[1]
$CC_{1/2}$	0.997 (0.644)[1]
Mean $I/\sigma(I)$	8.9 (1.5)[1]
Completeness (%)	99.8 (99.9)[1]
Multiplicity	5.7 (3.3)[1]
Wilson *B*-factor (Å^2)	10.868
Refinement	
Resolution (Å)	49.41-1.35 (1.37-1.35)[1]
No. of reflections	83856
R_{work}	0.1726
R_{free}	0.1880
R.m.s.d. from ideal geometry	
Bond lengths (Å)	0.007
Bond angles (°)	0.984
Ramachandran plot	
Most favored (%)	100.00
Allowed (%)	0.00
Outliers (%)	0.00
PDB code	9L8G

[1] Statistics in parentheses represent values calculated from the highest resolution shell.

Table. 7 Crystallographic data and refinement statistics of R115K mutant

	$R115K_{oxi}$	$R115K_{red}$
Data-collection statistics		
Beamline	SPring-8 BL44XU	SPring-8 BL44XU
Wavelength (Å)	0.90000	0.90000
Space group	$P3_221$	$P3_221$
Unit cell *a, b, c* (Å) α, β, γ (°)	58.95, 58.95, 186.87, 90, 90, 120	58.91, 58.91, 186.36, 90, 90, 120
Temperature (K)	100	100
Resolution (Å)	49.25-1.40 (1.42-1.40)[1]	44.75-1.44 (1.46-1.44)[1]
Total reflections	409998 (16807)[1]	444396 (17325)[1]
Unique reflections	75101 (3595)[1]	69004 (3368)[1]
R_{merge}	0.115 (0.646)[1]	0.076(0.515)[1]
R_{meas}	0.127 (0.727)[1]	0.082 (0.570)[1]
R_{pim}	0.053 (0.328)[1]	0.032 (0.238)[1]
$CC_{1/2}$	0.994 (0.742)[1]	0.998 (0.850)[1]
Mean $I/\sigma(I)$	8.0 (1.9)[1]	12.0 (2.2)[1]
Completeness (%)	99.8 (99.1)[1]	100.0 (99.0)[1]
Multiplicity	5.5 (4.7)[1]	6.4 (5.1)[1]
Wilson *B*-factor ($Å^2$)	10.5	13.1
Refinement		
Resolution (Å)	49.25-1.40 (1.42-1.40)[1]	34.40-1.44 (1.46-1.44)[1]
No. of reflections	75092	68993
R_{work}	0.1590	0.1749
R_{free}	0.1849	0.2034
R.m.s.d. from ideal geometry		
Bond lengths (Å)	0.006	0.006
Bond angles (°)	0.947	0.927
Ramachandran plot		
Most favored (%)	100.00	100.00
Allowed (%)	0.00	0.00
Outliers (%)	0.00	0.00

[1] Statistics in parentheses represent values calculated from the highest resolution shell.

(A) Oxidized state

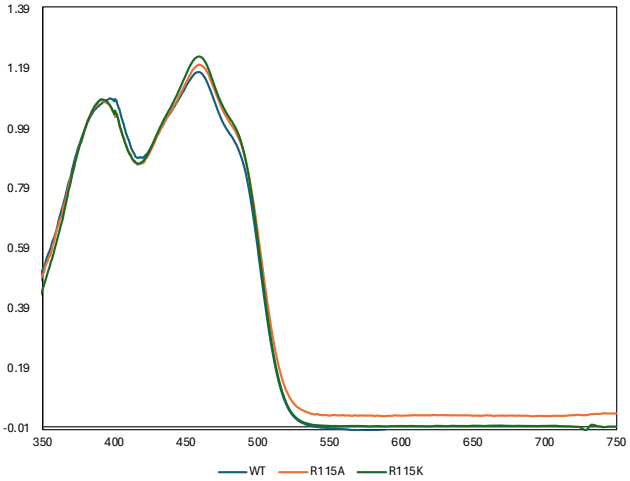

(B) Reduced state

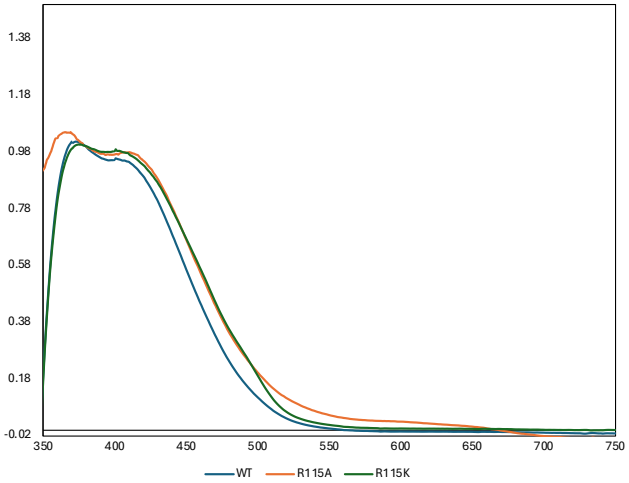

Figure 26. The absorption spectrum WT (blue), R115A (orange), R115K (green) of solution in each redox state. (A) Oxidized state. (B) Reduced state.

(A) Oxidized FAD in $wtFNR_{oxi}$

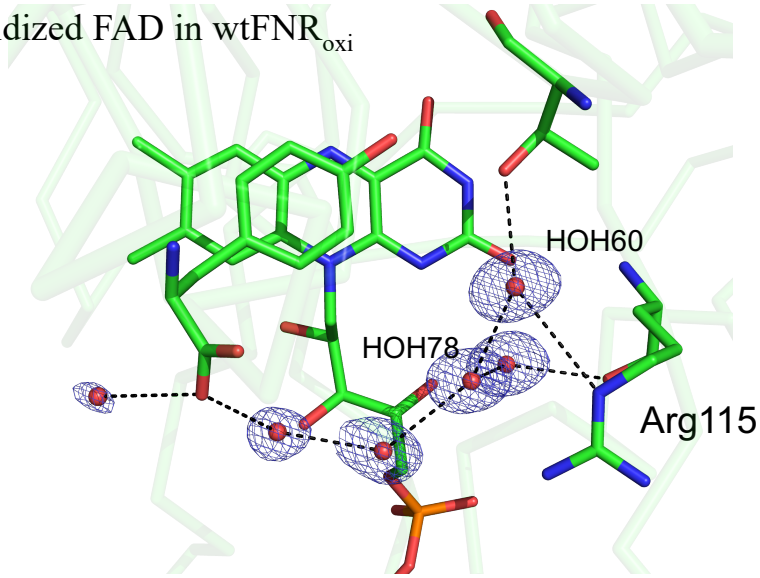

(B) Oxidized FAD in $mtFNR_{oxi}$

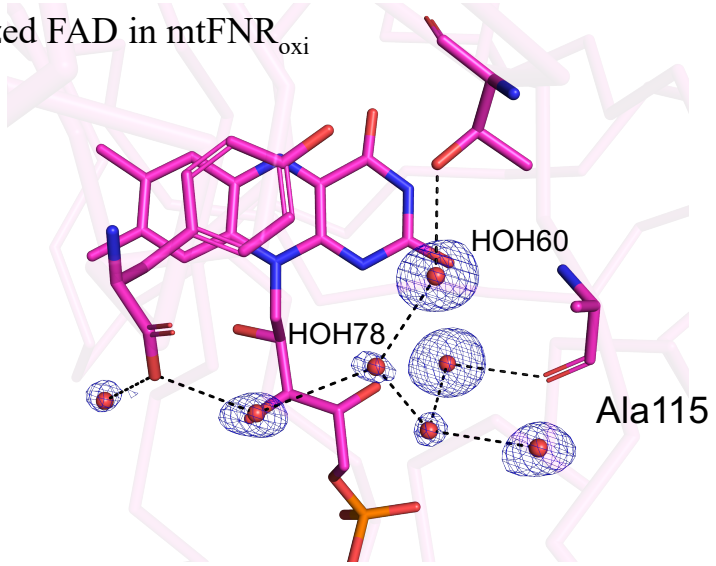

(C) Reduced $FADH_2$ in $wtFNR_{red}$

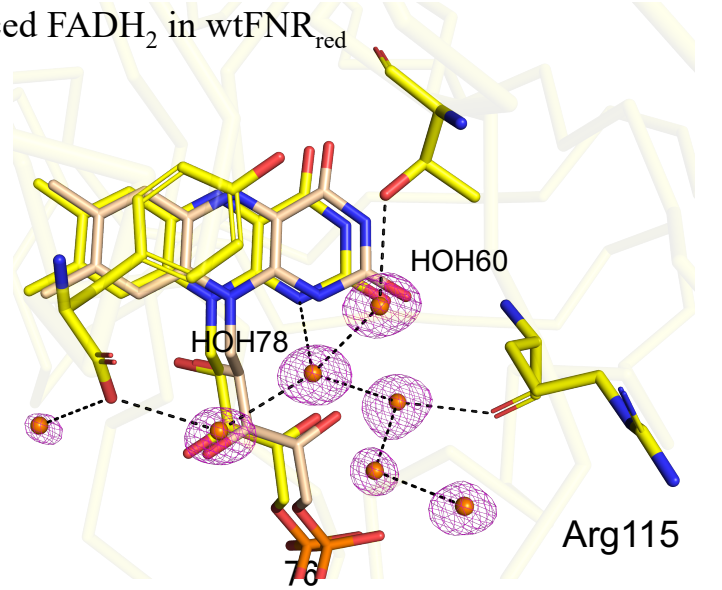

Figure 27. Water molecules arrangement around FAD. (A) Wild-type R-FNR oxidized form. Electron density (magenta mesh, 1.5σ contour level) maps for around FAD in oxidized form and the structure model determined in the present study. (B) R115A mutant R-FNR oxidized form. Electron density (blue mesh, 1.3σ contour level) maps for around FAD in oxidized form and the structure model determined in the present study.(C) Wild-type R-FNR reduced form. Electron density (magenta mesh, 1.5σ contour level) maps for around FAD in reduced form and the structure model determined in the present study. The black dash line is the hydrogen bond predicted by Ligplot (47).

(A) Oxidized FAD in $R115K_{oxi}$

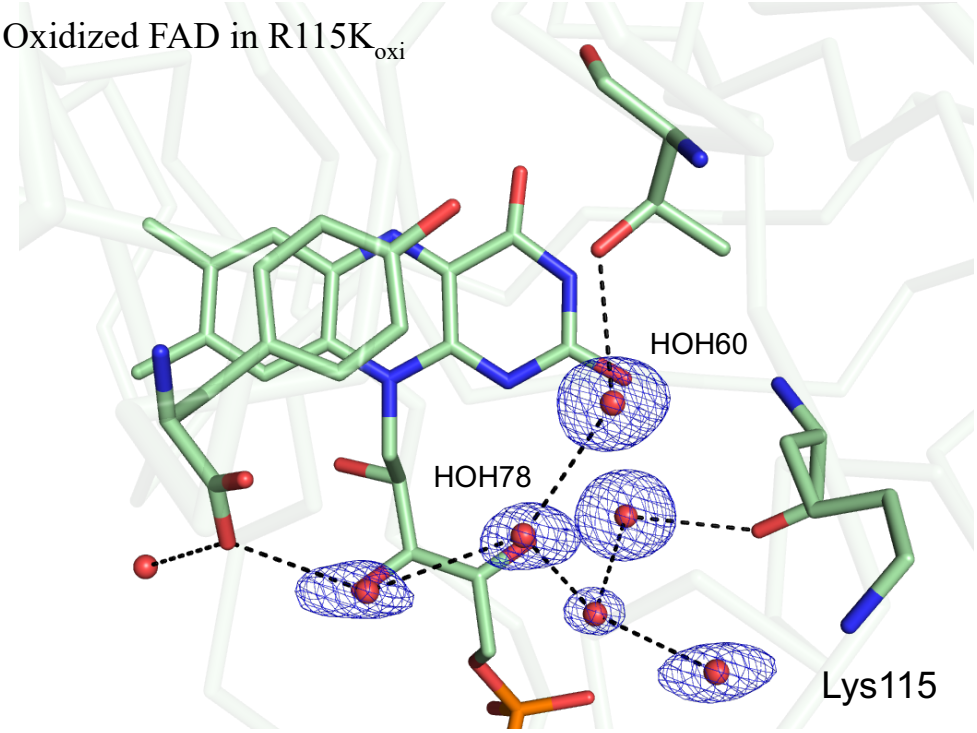

(B) Reduced $FADH_2$ in $R115K_{red}$

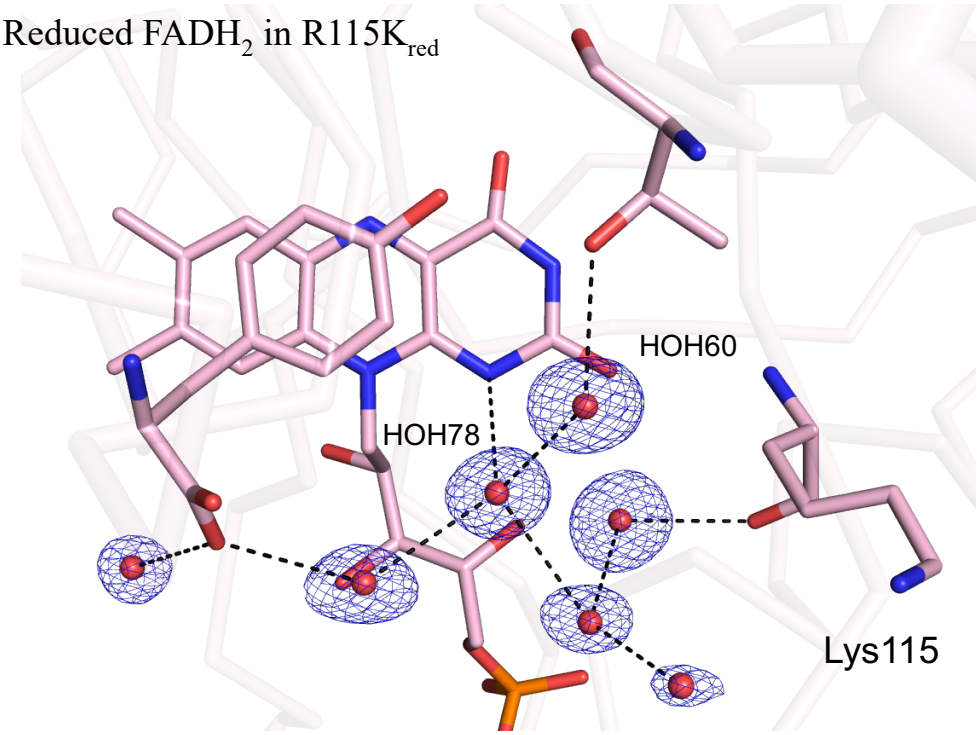

Figure 28. Water arrangement around FAD of R115 mutant. (A) R115K mutant R-FNR oxidized form. Electron density (blue mesh, 1.3σ contour level) maps for around FAD in oxidized form and the structure model determined in this study. (B) R115K mutant R-FNR reduced form. Electron density (magenta mesh, 1.3σ contour level) maps for around FAD in reduced form and the structure model determined in this study. The black dash line is the hydrogen bond predicted by Ligplot (47).

4-4 Discussion

As discussed in the Chapter III, the backbone structure showed no significant differences between the oxidized and reduced forms of wild-type FNR. When focusing on the water molecules surrounding FAD, the arrangement of water molecules in the oxidized R115A mutant ($R115_{oxi}$) closely resembled that of the reduced form of the wild-type. In the mutant, the absence of the Arg side chain prevented HOH60, which forms a hydrogen bond with the Arg115 side chain in the wild-type, from forming a hydrogen bond even in the oxidized state. As a result, the hydrogen-bond network around FAD in the mutant was maintained in a state similar to that of the reduced wild-type. This observation confirmed that the increased flexibility of Arg115 in the reduced form could be explained by a model of hydrogen-bond rearrangement mediated by water molecules.

In both $R115K_{oxi}$ and $R115K_{red}$ structures, the electron density for Lys115, except for its Cβ and Cγ atoms, was not clearly observed. This phenomenon is consistent with that previously observed in $wtFNR_{red}$, where the electron density of Arg115, except for its Cβ and Cγ atoms, was also absent. These findings suggest that this region exhibits high flexibility in both cases.

Furthermore, since Arg115 is replaced with Lys in Leaf-FNR, a comparison was conducted with the oxidized form of Leaf-FNR (PDB ID: 1gaw), which is currently available in the PDB. However, it should be noted that this structure was not determined with explicit consideration of X-ray radiation damage, and thus, a direct comparison should be interpreted with caution. In oxidized Leaf-FNR ($Leaf\text{-}FNR_{oxi}$), Lys116, which corresponds to Arg115, also exhibited a loss of electron density in its Cβ and Cγ atoms, adopting a structural conformation similar to that observed in the two mutant structures. This suggests that Lys115 in the R115K mutant exhibits structural behavior similar to that of Leaf-FNR.

To date, the reduced form of Leaf-FNR has not been reported. However, it is possible that Lys116 in L-FNR does not undergo redox-dependent structural changes, as observed for Arg115 in R-FNR. This inference is based on the fact that no significant structural changes have been observed in the oxidized and reduced states of Lys115 and its surrounding water molecules in R-FNR.

A previous study on maize R-FNR compared the intermolecular interaction strengths between photosynthetic and non-photosynthetic ferredoxins (Fd) and reported that non-photosynthetic FdIII, found in root plastids, has a dissociation constant (K_d) approximately 10 times lower than that of photosynthetic FdI (7). This finding suggests that the interaction mechanisms between photosynthetic and non-photosynthetic Fd-FNR pairs differ. The results obtained in this study indicate that the flexibility change in Arg115 is a phenomenon specific to R-FNR and suggest that it is a structural factor contributing to the high affinity for FdIII.

Additionally, a comparison of the water molecule arrangement around FAD was conducted. However, since the resolution of the structures used for comparison was 2.200 Å, the electron densities of the water molecules were not fully resolved. As a result, a detailed comparison of the hydrogen bond network around FAD was not feasible.

Finally, the potential impact of the increased mobility of the Arg115 side chain associated with redox change on complex formation was considered. A comparison was made with the non-physiological complex structure of oxidized Fd and oxidized FNR (PDB ID: 5h5j) reported in the previous study. The interface of this complex is characterized to be electrostatic: acidic residues on the Fd side and basic residues on the FNR side, strongly suggesting that the complex could be electrostatically stabilized even if one of the components were in the reduced state. Based on the precise structural analyses conducted in this study, it was found that the chemical reduction of

FAD to $FADH_2$ induces a rearrangement of the hydrogen-bond network, and this chemical formula change propagates to physical structural changes in Arg115. Arg115 is located on the molecular surface of FNR but does not directly interact with Fd in the complex structure reported previously (PDB ID: 5h5j); however, it modulates the positive electrostatic properties on the surface of FNR, thereby adjusting its affinity for Fd. This study proposes a regulatory mechanism in which Arg115 plays an indirect but crucial role in the redox-dependent interaction between FNR and Fd.

SUMMERY AND CONCLUSION

Ferredoxin-NADP$^+$ reductase (FNR) is a flavoprotein enzyme that binds flavin adenine dinucleotide (FAD) as a prosthetic group. In plant plastids, FNR catalyzes redox reactions between ferredoxin (Fd) and NADP(H). The isoalloxazine ring of FAD serves as the redox center, facilitating the transfer of two electrons. FAD can adopt three different chemical structures depending on its redox state: the oxidized form (FAD), the one-electron-reduced semiquinone form (FADH•), and the two-electron-reduced hydroquinone form ($FADH_2$). Structural changes induced by differences in these redox states of FAD are hypothesized to contribute to efficient interprotein electron transfer, including the association and dissociation between Fd and FNR. Consequently, numerous biochemical and structural biology studies have focused on the transient and specific complex formation of Fd and FNR. Enzymatic studies have reported significant differences in the *K*m values when comparing the activity of oxidized Fd with reduced FNR and the reverse reaction. However, due to experimental constraints, structural biology studies have primarily focused on the oxidized forms of both Fd and FNR. As a result, the detailed structural changes induced by the redox state of FAD and their effects on the interaction between Fd and FNR had not been thoroughly examined. To address this gap, this study employed X-ray crystallographic analyses under strict control of the redox states of FNR, using FNR derived from maize root, which yields high-quality structural information. Additionally, neutron crystallography, advantageous for visualizing hydrogen atoms, was employed to complement the findings.
In Chapter II, high-resolution X-ray crystallography was conducted with careful consideration of radiation damage. Obtaining high-resolution X-ray data requires increased X-ray exposure, which can generate solvated electrons that reduce the redox center. This phenomenon has been previously

reported and raises concerns about the reduction of FAD in oxidized FNR crystals during X-ray data collection. However, none of the FNR structures deposited in the Protein Data Bank had accounted for this issue. To ensure the analysis of the truly oxidized form, the relationship between X-ray exposure and FAD reduction rates was determined, and diffraction data were collected at the minimal exposure level where the reduction rate was below 10%. As a result, the oxidized structure of FNR was determined at a resolution of 1.15 Å. Additionally, the reduced structure of FNR, confirmed by micro-spectrophotometry, was determined at a resolution of 1.10 Å. A comparison of the two structures revealed no significant changes in the main chain. However, F_o - F_o difference Fourier maps calculated using the structure factors of the oxidized and reduced forms indicated that structural changes were concentrated around FAD, particularly in the side chains of Arg115 and Ser95 and in the C-terminal of Tyr317. Changes in the number and arrangement of surrounding water molecules were also observed. However, the mechanism by which these changes are linked to the reduction of FAD to $FADH_2$ could not be fully visualized, leaving only the hypothesis that they may result from altered hydrogen bonding between $FADH_2$ and the surrounding water molecules.

In Chapter III, neutron crystallography was conducted to accurately determine the positions of all atoms, including hydrogen atoms. A reproducible method for growing large crystals required for neutron crystallography was developed, and optimal freezing conditions for the crystals were established. Neutron diffraction data from both oxidized and reduced FNR were collected at 100 K using the TOF-Laue method at BL03 (iBIX) at J-PARC/MLF, achieving a resolution of 1.8 Å for both forms. The scattering length density derived from hydrogen atoms around FAD was successfully visualized, enabling the determination of the complete structures of FAD and $FADH_2$, including the positions of hydrogen atoms.

Additionally, the complex hydrogen-bond network formed by surrounding water molecules was elucidated, with clear distinctions between hydrogen bond donors and acceptors. Comparing the neutron structures of FNRs in oxidized and reduced forms revealed that the reduction of FAD to $FADH_2$ resulted in the formation of new, oblique hydrogen bonds involving the Oγ oxygen of Ser95 and the O atom of HOH78. This hydrogen bond formation influenced the positioning of Tyr317 relative to $FADH_2$. HOH78, in turn, formed hydrogen bonds with HOH60, which interacted with the side chain of Arg115. The rearrangement of the hydrogen bond network around HOH60, switching from an OH•••O donor-type to an O•••HO acceptor-type interaction, led to the disruption of the hydrogen bond with the Arg115 side chain and modulated its mobility. Arg115, located on the molecular surface of FNR, significantly influences the electrostatic properties critical for forming the electron transfer complex with Fd. These findings suggest that the rearrangement of hydrogen bonds induced by redox changes in FAD contributes to the distinct interactions between Fd and FNR.

In Chapter IV, to further investigate the structural function of Arg115 revealed in Chapters II and III, R115 mutants were generated. The oxidized structure of the R115A mutants was determined at a resolution of 1.35 Å, with careful consideration of X-ray radiation damage. The main chain structure of the mutant was highly similar to those of wild-type oxidized ($wtFNR_{oxi}$) and reduced ($wtFNR_{red}$) forms. Interestingly, the arrangement of water molecules around FAD in the oxidized structure of R115A mutant resembled that of the wild-type reduced structure, mimicking the disordered side chain of Arg115 observed in $wtFNR_{red}$. This confirmed that the water molecule configuration in the oxidized structure of R115A mutant closely resembled that of the wild-type reduced form.

The comprehensive results obtained through this study indicate that the subtle chemical formula changes by reduction of FAD to $FADH_2$ are

amplified into significant conformational changes in the side chain of Arg115. These changes are likely crucial for modulating the redox-state-dependent affinity of FNR for Fd. High-resolution X-ray and neutron structures of oxidized and reduced FNR were determined, revealing a novel mechanism by which the small chemical formula changes associated with the addition of two electrons and two protons to FAD are translated into large conformational changes in the side chains of Arg115 and Tyr317. These findings provide new insights into the structural basis for redox-regulated interactions between FNR and Fd.

REFERENCE

1. Knaff, D. B. (1996). Ferredoxin and ferredoxin-dependent enzymes. In Ort, D. R., & Yocum, C. F. (Eds.), Oxygenic photosynthesis: The light reactions (Advances in photosynthesis and respiration, Vol. 4, pp. 333–361). Springer, Dordrecht.
2. Hanke, G., & Mulo, P. (2013). Plant-type ferredoxins and ferredoxin-dependent metabolism. Plant, Cell and Environment, 36, 1071–1084. https://doi.org/10.1111/pce.12046
3. Goss, T., & Hanke, G. (2014). The end of the line: Can ferredoxin and ferredoxin NADP(H) oxidoreductase determine the fate of photosynthetic electrons? Current Protein & Peptide Science, 15(4), 385–393. 10.2174/1389203715666140327113733
4. Schultz, D. J., Suh, M. C., & Ohlrogge, J. B. (2000). Stearoyl-acyl carrier protein and unusual acyl-acyl carrier protein desaturase activities are differentially influenced by ferredoxin. *Plant Physiology*, 122(4), 907–916. 10.1104/pp.124.2.681
5. Brouquisse, R., Weigel, P., Rhodes, D., Yocum, C. F., & Hanson, A. D. (1989). Evidence for a ferredoxin-dependent choline monooxygenase from spinach chloroplast stroma. *Plant Physiology*, 90(1), 322–329. 10.1104/pp.90.1.322
6. Muramoto, T., Kohchi, T., Yokota, A., Hwang, I., & Goodman, H. M. (1999). The Arabidopsis photomorphogenic mutant hy1 is deficient in phytochrome chromophore biosynthesis as a result of a mutation in a plastid heme oxygenase. *The Plant Cell*, 11(2), 335–347.10.1105/tpc.11.3.335
7. Onda, Y., Matsumura, T., Kimata-Ariga, Y., Sakakibara, H., Sugiyama, T., & Hase, T. (2000). Differential interaction of maize root ferredoxin:$NADP^+$ oxidoreductase with photosynthetic and non-

photosynthetic ferredoxin isoproteins. *Plant Physiology*, 123(3), 1037–1046. https://doi.org/10.1104/pp.123.3.1037

8. Hanke, G. T., Kurisu, G., Kusunoki, M., & Hase, T. (2004). Fd:FNR electron transfer complexes: Evolutionary refinement of structural interactions. *Photosynthesis Research*, 81, 317–327. 10.1023/B:PRES.0000036885.01534.b8
9. Flores, E., Frías, J. E., Rubio, L. M., & Herrero, A. (2005). Photosynthetic nitrate assimilation in cyanobacteria. *Photosynthesis Research*, 83, 117–133. 10.1007/s11120-004-5830-9
10. Yonekura-Sakakibara, K., Onda, Y., Ashikari, T., Tanaka, Y., Kusumi, T., & Hase, T. (2000). Analysis of reductant supply systems for ferredoxin-dependent sulfite reductase in photosynthetic and nonphotosynthetic organs of maize. *Plant Physiology*, 122(3), 887–894. https://doi.org/10.1104/pp.122.3.887
11. Bowsher, C. G., Dunbar, B., & Emes, M. J. (1993). The purification and properties of ferredoxin-$NADP^+$-oxidoreductase from roots of *Pisum sativum* L. *Protein Expression and Purification*, 4(4), 512–518. 10.1006/prep.1993.1067
12. Hanke, G. T., Endo, T., Satoh, F., & Hase, T. (2008). Altered photosynthetic electron channelling into cyclic electron flow and nitrite assimilation in a mutant of ferredoxin:NADP(H) reductase. *Plant, Cell and Environment*, 31(7), 1017–1028. https://doi.org/10.1111/j.1365-3040.2008.01814.x
13. Kim, J. Y., Nakayama, M., Toyota, H., Kurisu, G., & Hase, T. (2016). Structural and mutational studies of an electron transfer complex of maize sulfite reductase and ferredoxin. *The Journal of Biochemistry*, 160(2), 101–109. https://doi.org/10.1093/jb/mvw016
14. Sakakibara, Y., Kimura, H., Iwamura, A., Saitoh, T., Ikegami, T., Kurisu, G., & Hase, T. (2012). A new structural insight into differential

interaction of cyanobacterial and plant ferredoxins with nitrite reductase as revealed by NMR and X-ray crystallographic studies. *The Journal of Biochemistry*, 151(5), 483–492. https://doi.org/10.1093/jb/mvs028

15. Glauser, D. A., Bourquin, F., Manieri, W., & Schürmann, P. (2004). Characterization of ferredoxin:thioredoxin reductase modified by site-directed mutagenesis. *Journal of Biological Chemistry*, 279(16), 16662–16669. https://doi.org/10.1074/jbc.M313851200
16. Kurisu, G., Kusunoki, M., Katoh, E., Yamazaki, T., Teshima, K., Onda, Y., Kimata-Ariga, Y., & Hase, T. (2001). Structure of the electron transfer complex between ferredoxin and ferredoxin-$NADP^+$ reductase. *Nature Structural Biology*, 8, 117–121. 10.1038/84097
17. Shinohara, F., Kurisu, G., Hanke, G., Bowsher, C., Hase, T., & Kimata-Ariga, Y. (2017). Structural basis for the isotype-specific interactions of ferredoxin and ferredoxin:$NADP^+$ oxidoreductase: An evolutionary switch between photosynthetic and heterotrophic assimilation. *Photosynthesis Research*, 134(2), 291–299. 10.1007/s11120-016-0331-1
18. Kinoshita, M., Kim, J. Y., Kume, S., Lin, Y., Mok, K. H., Kataoka, Y., Ishimori, K., Markova, N., Kurisu, G., Hase, T., & Lee, Y. H. (2017). Energetic basis on interactions between ferredoxin and ferredoxin $NADP^+$ reductase at varying physiological conditions. *Biochemical and Biophysical Research Communications*, 483(1), 262–267. https://doi.org/10.1016/j.bbrc.2016.11.132
19. Chikuma, Y., Miyata, M., Lee, Y.-H., Hase, T., & Kimata-Ariga, Y. (2021). Molecular mechanism of negative cooperativity of ferredoxin-$NADP^+$ reductase by ferredoxin and NADP(H): Involvement of a salt bridge between Asp60 of ferredoxin and Lys33 of FNR. *Bioscience, Biotechnology, and Biochemistry*, 85(4), 860–865. 10.1093/bbb/zbaa102
20. Kurisu, G., Nishiyama, D., Kusunoki, M., Fujikawa, M., Ikeuchi, M., & Tamada, T. (2005). A structural basis of *Equisetum arvense* ferredoxin

isoform II producing an alternative electron transfer with ferredoxin-$NADP^+$ reductase. *Journal of Biological Chemistry*, 280(3), 2275–2281. https://doi.org/10.1074/jbc.M408904200

21. Teshima, K., Fujita, S., Hirose, S., Nishiyama, T., Matsumura, T., & Hase, T. (2003). A ferredoxin Arg-Glu pair important for efficient electron transfer between ferredoxin and ferredoxin-$NADP^+$ reductase. *FEBS Letters*, 546(2-3), 189–194. 10.1016/s0014-5793(03)00559-3
22. Deng, Z., Aliverti, A., Zanetti, G., Arakaki, A. K., Ottado, J., Orellano, E. G., Calcaterra, N. B., Ceccarelli, E. A., Carrillo, N., & Karplus, P. A. (1999). A productive $NADP^+$ binding mode of ferredoxin–NADP+ reductase revealed by protein engineering and crystallographic studies. *Nature Structural Biology*, 6, 847–853. 10.1038/12307
23. Kean, K. M., Carpenter, R. A., Pandini, V., Zanetti, G., Hall, A. R., Faber, R., Aliverti, A., & Karplus, P. A. (2017). High-resolution studies of hydride transfer in the ferredoxin:$NADP^+$ reductase superfamily. *The FEBS Journal*, 284(20), 3288–3307. 10.1111/febs.14190
24. Garman, E. F. (2010). Radiation damage in macromolecular crystallography: What is it and why should we care? *Acta Crystallographica Section D*, 66(4), 339–351. 10.1107/S0907444910008656
25. Ohnishi, Y., Muraki, N., Kiyota, D., Okumura, H., Baba, S., Kawano, Y., Kumasaka, T., Tanaka, H., & Kurisu, G. (2020). X-ray dose-dependent structural changes of the [2Fe-2S] ferredoxin from *Chlamydomonas reinhardtii*. *The Journal of Biochemistry*, 167(6), 549–555. https://doi.org/10.1093/jb/mvaa045
26. Niimura, N., & Podjarny, A. (2011). *Neutron protein crystallography: Hydrogen, protons, and hydration in bio-macromolecules*. Oxford University Press, Oxford, United Kingdom.

27. Ueno, G., Kanda, H., Hirose, R., Ida, K., Kumasaka, T., & Yamamoto, M. (2006). RIKEN structural genomics beamlines at the SPring-8: High throughput protein crystallography with automated beamline operation. *J. Struct. Funct. Genomics, 7*, 15–22. https://doi.org/10.1007/s10969-005-9005-5
28. Ueno, G., Kanda, H., Kumasaka, T., & Yamamoto, M. (2005). Development of an automatic data collection system at the RIKEN structural genomics beamline. *J. Synchrotron Rad.*, 12, 380–384. https://doi.org/10.1107/S0909049505004735
29. Brockhauser, S., Ravelli, R. B. G., & McCarthy, A. A. (2013). The use of an automatic data processing pipeline for macromolecular crystallography. *J. Appl. Cryst.*, 46, 1225–1230. https://doi.org/10.1107/S0021889813011461
30. Kabsch, W. (2010). XDS. Acta Cryst. D, 66, 125–132. 10.1107/S0907444909047337
31. McCoy, A. J., Grosse-Kunstleve, R. W., Adams, P. D., Winn, M. D., Storoni, L. C., & Read, R. J. (2007). Phaser crystallographic software. *J. Appl. Cryst.*, 40, 658–674. 10.1107/S0021889807021206
32. Afonine, P. V., Grosse-Kunstleve, R. W., Echols, N., Headd, J. J., Moriarty, N. W., Mustyakimov, M., Terwilliger, T. C., Urzhumtsev, A., Zwart, P. H., & Adams, P. D. (2012). Towards automated crystallographic structure refinement with phenix.refine. *Acta Cryst. D*, 68, 352–367. 10.1107/S0907444912001308
33. Adams, P. D., Afonine, P. V., Bunkóczi, G., Chen, V. B., Davis, I. W., Echols, N., Headd, J. J., Hung, L.-W., Kapral, G. J., Grosse-Kunstleve, R. W., McCoy, A. J., Moriarty, N. W., Oeffner, R., Read, R. J., Richardson, D. C., Richardson, J. S., Terwilliger, T. C., & Zwart, P. H. (2010). PHENIX: A comprehensive Python-based system for

macromolecular structure solution. *Acta Crystallographica Section D*, 66(2), 213–221. 10.1107/S0907444909052925

34. Emsley, P., Lohkamp, B., Scott, W. G., & Cowtan, K. (2010). Features and development of Coot. Acta Cryst. D, 66, 486– 501 10.1107/S0907444910007493
35. Agirre, J., Murshudov, G. N., Turkenburg, J. P., Dodson, E. J., & Wilson, K. S. (2023). The CCP4 suite: integrative software for macromolecular crystallography. Acta Cryst. D, 79, 449–461. 10.1107/S2059798323003595
36. Tanaka, I., Kusaka, K., Tomoyori, K., Niimura, N., Ohhara, T., Kurihara, K., Kuroki, R., & Ishikawa, T. (2009). Overview of a new biological neutron diffractometer (iBIX) in J-PARC. *Nucl. Instrum. Methods Phys. Res. A*, 600, 161–163. https://doi.org/10.1016/j.nima.2008.11.134
37. Tanaka, I., Kusaka, K., Hosoya, T., Niimura, N., Ohhara, T., Kurihara, K., Kuroki, R., & Ishikawa, T. (2010). Neutron structure analysis using the IBARAKI biological crystal diffractometer (iBIX) at J-PARC. *Acta Cryst. D*, 66, 1194–1197. https://doi.org/10.1107/S0907444910031422
38. Kusaka, K., Hosoya, T., Yamada, T., Tomoyori, K., Ohhara, T., Katagiri, M., Kuroki, R., & Tanaka, I. (2013). Evaluation of performance for IBARAKI biological crystal diffractometer iBIX with new detectors. J. Synchrotron Radiat., 20, 994–998. 10.1107/S0909049513021845
39. Hosoya, T., Nakamura, T., Katagiri, M., Birumachi, A., Ebine, M., & Soyama, K. (2009). Development of a new detector and DAQ systems for iBIX. *Nucl. Instrum. Methods Phys. Res. A*, 600, 217–219. https://doi.org/10.1016/j.nima.2008.11.123
40. Yano, N., Yamada, T., Hosoya, T., Ohhara, T., Tanaka, I., Niimura, N., Kuroki, R., & Kurihara, K. (2018). Status of the neutron time-of-flight single-crystal diffraction data-processing software STARGazer. *Acta Cryst. D*, 74, 1041–1052. https://doi.org/10.1107/S2059798318014606

41. Ohhara, T., Kusaka, K., Hosoya, T., Kurihara, K., Tomoyori, K., Niimura, N., Tanaka, I., Kuroki, R., & Ishikawa, T. (2009). Development of data processing software for a new TOF single crystal neutron diffractometer at J-PARC. *Nuclear Instruments and Methods in Physics Research Section A: Accelerators, Spectrometers, Detectors and Associated Equipment*, 600(1), 195–197.
42. Kusaka, K., Yokoyama, T., Yamada, T., Yano, N., Tanaka, I., & Mizuguchi, M. (2020). Neutron diffraction experiment with the Y116S variant of transthyretin using iBIX at J-PARC: application of a new integration method. *Acta Cryst. D*, 76, 1050–1056. https://doi.org/10.1107/S2059798320011835
43. Yamashita, K., Wojdyr, M., Long, F., Nicholls, R. A., & Murshudov, G. N. (2023). GEMMI and Servalcat restrain REFMAC5. *Acta Cryst. D*, 79 (Pt 5), 368–373. https://doi.org/10.1107/S2059798323002413
44. Catapano, L., Long, F., Yamashita, K., Nicholls, R. A., Steiner, R. A., & Murshudov, G. N. (2023). Neutron crystallographic refinement with REFMAC5 from the CCP4 suite. *Acta Cryst. D*, 79 (Pt 12), 1056–1070. https://doi.org/10.1107/S2059798323008793
45. Bruns, C. M., & Karplus, P. A. (1995). Refined crystal structure of spinach ferredoxin reductase at 1.7 Å resolution: Oxidized, reduced, and 2'-phospho-5'-AMP bound states. *Journal of Molecular Biology*, 247(1), 125–145. 10.1006/jmbi.1994.0127
46. Correll, C. C., Ludwig, M. L., Bruns, C. M., & Karplus, P. A. (1993). Structural prototypes for an extended family of flavoprotein reductases: Comparison of phthalate dioxygenase reductase with ferredoxin reductase and ferredoxin. *Protein Science*, 2(12), 2112–2133.10.1002/pro.5560021212
47. Wallace, A. C., Laskowski, R. A., & Thornton, J. M. (1995). LIGPLOT: A program to generate schematic diagrams of protein-ligand interactions.

Protein Engineering, Design & Selection, 8(2), 127–134. 0.1093/protein/8.2.127

48. Schwinn, K., Morlot, C., Mony, J., Franz, S., Ritz, T., Brettel, K., & Gauduel, Y. (2020). UV-visible absorption spectrum of FAD and its reduced forms embedded in a cryptochrome protein. *Physical Chemistry Chemical Physics*, 22, 12447–12455. 10.1039/D0CP01714K

PUBLICATION

Midori Uenaka, Yusuke Ohnishi, Akane Ise, Jiang Yu, Naomine Yano, Katsuhiro Kusaka, Hideaki Tanaka, Genji Kurisu.

Redox-dependent hydrogen bond network rearrangement of Ferredoxin-$NADP^+$ reductase revealed by high-resolution X-ray and neutron crystallography

Acta Crystallographica Section F:Structural Biology Communications, 2025, F81(3), 73-84. 10.1107/S2053230X25000524